

A 38 Million Year Old Mini-Neptune in the Kepler Field

² L. G. BOUMA,^{1,2,*} J. L. CURTIS,^{3,4} K. MASUDA,⁵ L. A. HILLENBRAND,¹ G. STEFANSSON,^{2,†} H. ISAACSON,⁶
³ N. NARITA,^{7,8,9,10} A. FUKUI,^{7,10} M. IKOMA,¹¹ M. TAMURA,^{12,9,11} A. L. KRAUS,¹³ E. FURLAN,¹⁴
⁴ C. L. GNILKA,^{15,14} K. V. LESTER,¹⁵ AND S. B. HOWELL¹⁵

⁵ Cahill Center for Astrophysics, California Institute of Technology, Pasadena, CA 91125, USA

⁶ Department of Astrophysical Sciences, Princeton University, 4 Ivy Lane, Princeton, NJ 08540, USA

⁷ Department of Astronomy, Columbia University, 550 West 120th Street, New York, NY 10027, USA

⁸ Department of Astrophysics, American Museum of Natural History, New York, NY 10024, USA

⁹ Department of Earth and Space Science, Osaka University, Osaka 560-0043, Japan

¹⁰ Astronomy Department, University of California, Berkeley, CA 94720, USA

¹¹ Komaba Institute for Science, The University of Tokyo, Tokyo 153-8902, Japan

¹² Japan Science and Technology Agency, PRESTO, Tokyo 153-8902, Japan

¹³ Astrobiology Center, Tokyo 181-8588, Japan

¹⁴ Instituto de Astrofísica de Canarias (IAC), 38205 La Laguna, Tenerife, Spain

¹⁵ Division of Science, National Astronomical Observatory of Japan, Tokyo 181-8588, Japan

¹⁶ Department of Astronomy, The University of Tokyo, Tokyo 113-0033, Japan

¹⁷ Department of Astronomy, The University of Texas at Austin, Austin, TX 78712, USA

¹⁸ NASA Exoplanet Science Institute, Caltech/IPAC, Pasadena, CA 91125, USA

¹⁹ NASA Ames Research Center, Moffett Field, CA 94035, USA

(Received 2021 Oct 12; Revised —; Accepted —)

Submitted to AAS Journals

ABSTRACT

Kepler 1627A is a G8V star previously known to host a $3.8 R_{\oplus}$ mini-Neptune on a 7.2 day orbit. The star was observed by the Kepler space telescope because it is nearby ($d = 329$ pc) and it resembles the Sun. Here we show using Gaia kinematics, TESS stellar rotation periods, and spectroscopic lithium abundances that Kepler 1627 is a member of the 38^{+6}_{-5} Myr old δ Lyr cluster. To our knowledge, this makes Kepler 1627Ab the youngest planet with a precise age yet found by the main Kepler mission. The Kepler photometry shows two peculiarities: the average transit profile is asymmetric, and the individual transit times might be correlated with the local light curve slope. We discuss possible explanations for each anomaly. More importantly, the δ Lyr cluster is one of $\sim 10^3$ coeval groups whose properties have been clarified by Gaia. Many other exoplanet hosts are candidate members of these clusters; their ages can be verified (**Replaced: through replaced with: with**) the trifecta of Gaia, TESS, and ground-based spectroscopy.

Keywords: exoplanet evolution (491), open star clusters (1160), stellar ages (1581)

1. INTRODUCTION

While thousands of exoplanets have been discovered orbiting nearby stars, the vast majority of them are several billion years old. This makes it

difficult to test origin theories for the different families of planets, since many evolutionary processes are expected to operate on timescales of less than 100 million years.

For instance, the “mini-Neptunes”, thought to be made of metal cores, silicate mantles (Kite et al. 2020), and extended hydrogen-dominated atmospheres, are expected to shrink in size by factors of several over their first 10^8 years. Specifically, in the models of Owen & Wu (2016) and

Corresponding author: L. G. Bouma
luke@astro.caltech.edu

* 51 Pegasi b Fellow

† Henry Norris Russell Fellow

Owen (2020), the $\approx 5 M_{\oplus}$ planets start with sizes of $4 - 12 R_{\oplus}$ shortly after the time of disk dispersal ($\lesssim 10^7$ years), and shrink to sizes of $2 - 4 R_{\oplus}$ by 10^8 years. While the majority of this change is expected to occur within the first few million years after the disk disperses (Ikoma & Hori 2012), stellar irradiation and internal heat can also power gradual outflows which, if strong enough, can deplete or entirely strip the atmosphere (Lopez et al. 2012; Owen & Wu 2013; Ginzburg et al. 2018). Discovering young planets, measuring their masses, and detecting their atmospheric outflows are key steps toward testing this paradigm, which is often invoked to explain the observed radius distribution of mature exoplanets (Fulton et al. 2017; Van Eylen et al. 2018).

The K2 and TESS missions have now enabled the detection of about ten close-in planets younger than 100 million years, all smaller than Jupiter (Mann et al. 2016; David et al. 2016, 2019; Newton et al. 2019; Bouma et al. 2020; Plavchan et al. 2020; Rizzuto et al. 2020; Martioli et al. 2021). The Kepler mission however has not yielded any planets with precise ages below one gigayear (Meibom et al. 2013). The reason is that during the main Kepler mission (2009–2013), only four open clusters were known in the Kepler field, with ages spanning 0.7 Gyr to 9 Gyr (Meibom et al. 2011). Though isochronal, gyrochronal, and lithium-based analyses suggest that younger Kepler planets do exist (Walkowicz & Basri 2013; Berger et al. 2018; David et al. 2021), accurate and precise age measurements typically require an ensemble of stars. Fortunately, recent analyses of the Gaia data have greatly expanded our knowledge of cluster memberships (e.g., Cantat-Gaudin et al. 2018; Zari et al. 2018; Kounkel & Covey 2019; Meingast et al. 2021; Kerr et al. 2021). As part of our Cluster Difference Imaging Photometric Survey (CDIPS, Bouma et al. 2019), we concatenated the available analyses from the literature, which yielded a list of candidate young and age-dated stars (see Appendix A).

Matching our young star list against stars observed by Kepler revealed that Kepler observed a portion of the δ Lyr cluster (Stephenson-1; Theia 73). More specifically, a clustering analysis of the Gaia data by Kounkel & Covey (2019) reported that Kepler 1627 (KIC 6184894; KOI 5245) is a δ Lyr cluster member. Given the previous statistical validation of the close-in mini-Neptune Kepler 1627b (Tenenbaum et al. 2012; Morton et al. 2016; Thompson et al. 2018), we begin by scrutinizing the properties of the cluster (Section 2). We find that the δ Lyr cluster is 38^{+6}_{-5} Myr old, and in Section 3 show that Kepler 1627 is both a binary and also a member of the cluster. Focusing on the

planet (Section 4), we confirm that despite the existence of the previously unreported M2.5V companion, hereafter Kepler 1627B, the planet orbits the G-dwarf primary, Kepler 1627A. We also analyze an asymmetry in the average transit profile, and a possible correlation between the individual transit times and the local light curve slope. We conclude by discussing broader implications for our ability to age-date a larger sample of planets (Section 5).

2. THE CLUSTER

To measure the age of the δ Lyr cluster, we first selected a set of candidate cluster members (Section 2.1), and then analyzed these stars using a combination of the isochronal and gyrochronal techniques (Section 2.2).

2.1. Selecting Cluster Members

Kounkel & Covey (2019) applied an unsupervised clustering algorithm to Gaia DR2 on-sky positions, proper motions, and parallaxes for stars within the nearest kiloparsec. For the δ Lyr cluster (Theia 73), they reported 3,071 candidate members. We matched these stars against the latest Gaia EDR3 observations using the dr2_neighbourhood table from the ESA archive, taking the stars closest in proper motion and epoch-corrected angular distance as the presumed match (Gaia Collaboration et al. 2021a). In Figure 1, have shown galactic positions only for the stars with parallax signal-to-noise exceeding 20. The reported cluster members (gray and black points) extend over a much larger volume than the cluster previously identified by Stephenson (1959) and later corroborated by Eggen (1968). While the non-uniform “clumps” of stars might comprise a *bona fide* cluster of identically-aged stars, they could also be heavily contaminated by field stars. We therefore considered stars only in the immediate kinematic and spatial vicinity of Kepler 1627 as candidate cluster members. We performed the selection cuts manually, by drawing lassos with the interactive glue visualization tool (Beaumont et al. 2014) in the four projections shown in Figure 1. The overlap between the Kepler field and the resulting candidate cluster members is shown in Figure 2. While this method will include some field interlopers in the “cluster star” sample, and vice-versa, it should suffice for our aim of verifying the existence of the cluster in the vicinity of Kepler 1627.

2.2. The Cluster’s Age

2.2.1. Color-Absolute Magnitude Diagram

We measured the isochrone age using an empirical approach. The left panel of Figure 3 shows the color-absolute magnitude diagram (CAMD) of

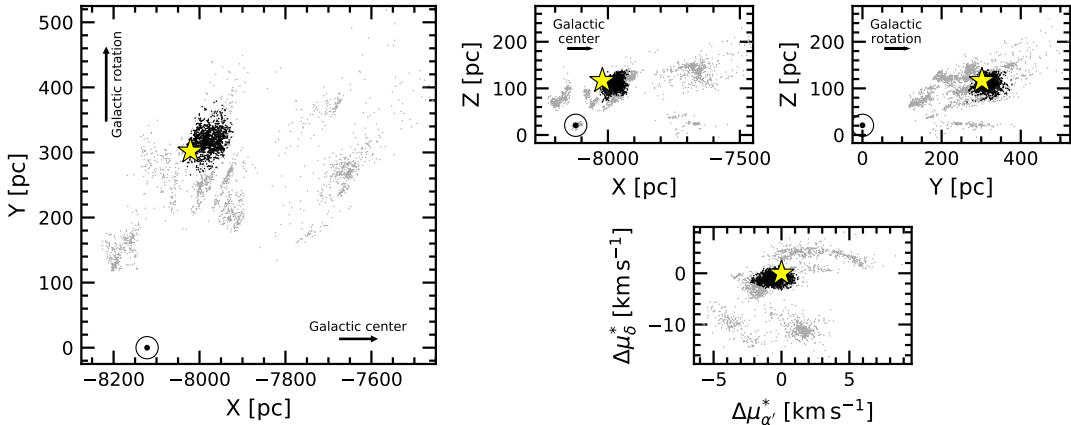


Figure 1. Galactic positions and tangential velocities of stars in the δ Lyr cluster. Points are reported cluster members from Kounkel & Covey (2019). The tangential velocities relative to Kepler 1627 (bottom right) are computed assuming that every star has the same three-dimensional spatial velocity as Kepler 1627. Our analysis considers stars (black points) in the spatial and kinematic vicinity of Kepler 1627 (yellow star). The question of whether the other candidate cluster members (gray points) are part of the cluster is outside our scope. The location of the Sun (\odot) is shown.

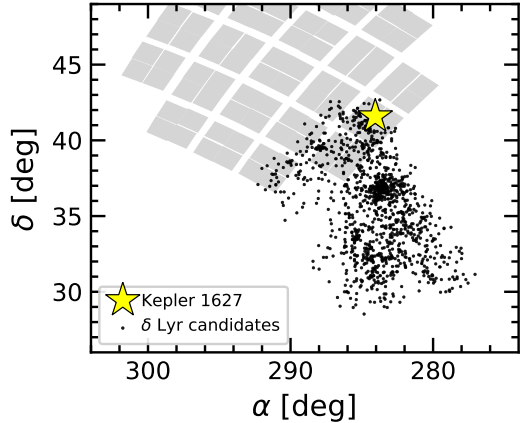


Figure 2. Kepler's view of the δ Lyr cluster, shown in equatorial coordinates. Each black circle is a candidate cluster member selected based on its position and kinematics (Figure 1). Of the 1,201 candidate cluster members, 58 have at least one quarter of Kepler data. TESS has also observed most of the cluster, for one to two lunar months to date.

candidate δ Lyr cluster members, IC 2602, the Pleiades, and the field. The stars from the Pleiades and IC 2602 were adopted from Cantat-Gaudin et al. (2018), and the field stars are from the Gaia EDR3 Catalog of Nearby Stars (Gaia Collaboration et al. 2021b). We cleaned these following the data filtering criteria from Gaia Collaboration et al. (2018a, Appendix B), except that we weakened the parallax precision requirement to $\varpi/\sigma_\varpi > 5$. (Added: This also involved cuts on the photometric signal to noise ratio, the number of visibility periods used, the astrometric χ^2 of the single-source solution, and the $G_{\text{BP}} - G_{\text{RP}}$ color excess factor.) These filters were designed

to include genuine binaries while omitting instrumental artifacts. We then corrected for extinction by querying the 3-dimensional maps of Capitanio et al. (2017) and Lallement et al. (2018)¹, and applied the extinction coefficients $k_X \equiv A_X/A_0$ computed by Gaia Collaboration et al. (2018a) assuming that $A_0 = 3.1E(B-V)$. For IC 2602, the Pleiades, and the δ Lyr cluster, this procedure yielded a respective mean and standard deviation for the reddening of $E(B-V) = \{0.020 \pm 0.003, 0.045 \pm 0.008, 0.032 \pm 0.006\}$. These values (Replaced: agree reasonably well with replaced with: are within a factor of two of) previously reported values (Replaced: from replaced with: in) the literature (e.g., Gaia Collaboration et al. 2018a; Kounkel & Covey 2019; Bossini et al. 2019)(Added: , and are all small enough that the choice of whether to use them vs. other extinction estimates does not affect our primary conclusions).

Figure 3 shows that the δ Lyr cluster and IC 2602 overlap, and therefore are approximately the same age. In our exploration, we also compared against μ -Tau (62 ± 7 Myr; Gagné et al. 2020) and the Upper-Centaurus-Lupus (UCL) component of the Sco OB2 association (≈ 16 Myr; Pecaut & Mamajek 2016). The pre-main-sequence M dwarfs of the δ Lyr cluster were intermediate between the latter two clusters. To turn this heuristic interpolation into an age measurement, we used the empirical method developed by Gagné et al. (2020). In brief, we fitted the pre-main-sequence loci of a set of reference clusters, and the locus of the target δ Lyr cluster was then modeled as a piecewise linear

¹ <https://stilism.obspm.fr/>, 2021/09/25

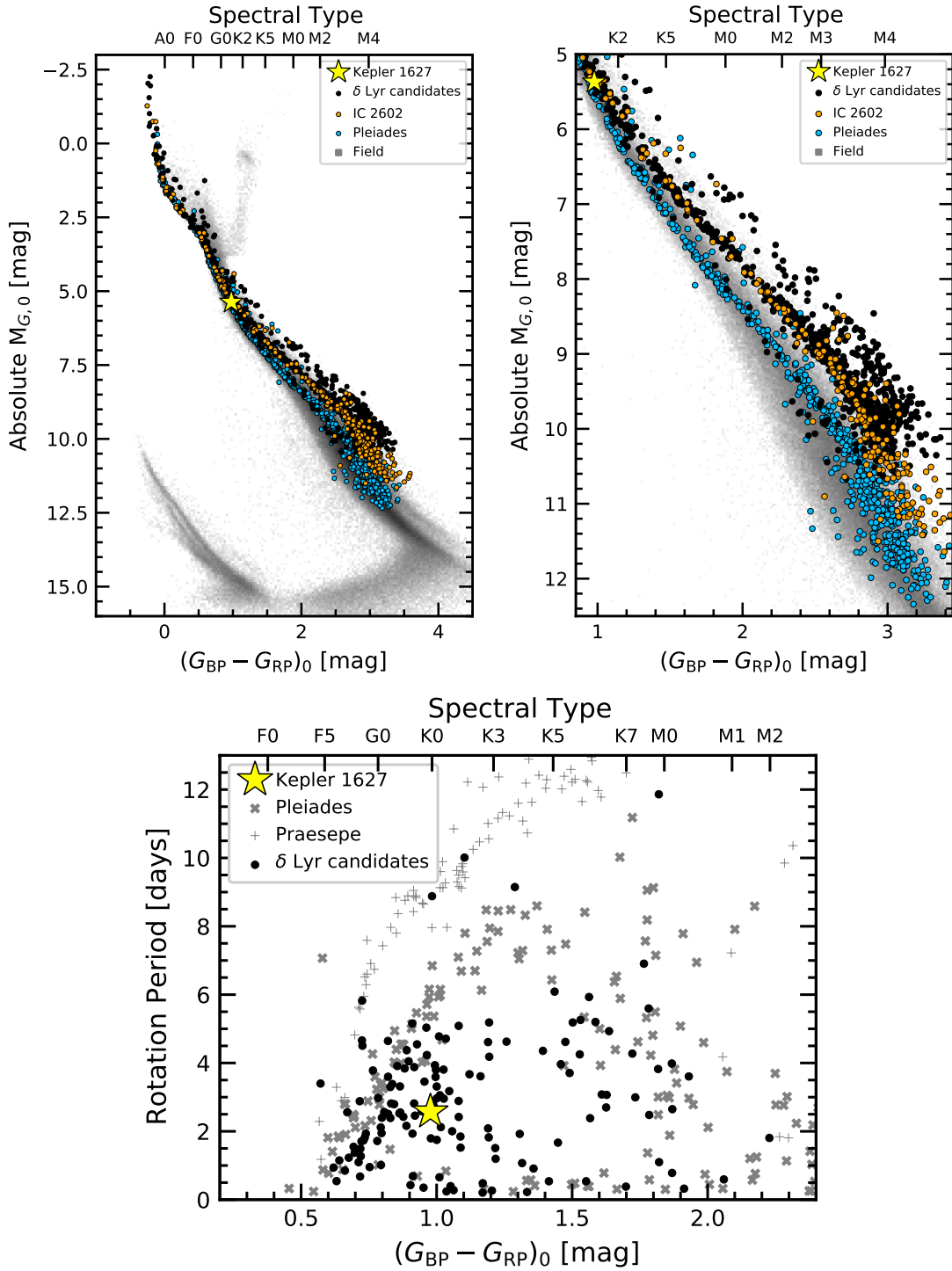


Figure 3. The δ Lyr cluster is 38^{+6}_{-5} Myr old. *Top:* Color-absolute magnitude diagram of candidate δ Lyr cluster members, in addition to stars in IC 2602 (≈ 38 Myr), the Pleiades (≈ 115 Myr), and the Gaia EDR3 Catalog of Nearby Stars (gray background). The zoomed right panel highlights the pre-main-sequence. The δ Lyr cluster and IC 2602 are approximately the same isochronal age. *Bottom:* TESS and Kepler stellar rotation period versus dereddened Gaia color, with the Pleiades and Praesepe (650 Myr) shown for reference (Rebull et al. 2016; Douglas et al. 2017). Most candidate δ Lyr cluster members are gyrochronologically younger than the Pleiades; outliers are probably field interlopers.

combination of these reference clusters. For our reference clusters, we adopted members of UCL, IC 2602, and the Pleiades from Damiani et al. (2019) and Cantat-Gaudin et al. (2018) respectively. We removed binaries by requiring RUWE < 1.3, `radial_velocity_error` below the 80th percentile of each cluster's distribution, and excluded stars that were obvious photometric binaries in the CAMD.² We then passed a moving box average and standard deviation across the CAMD in 0.10 mag bins, fitted a univariate spline to the binned values, and assembled a piecewise grid of (**Deleted:** `hybrid`) isochrones spanning the ages between UCL (**Replaced:** `to` replaced with: `and`) the Pleiades using Equation(**Replaced:** `s 6 and 7` replaced with: `6`) from Gagné et al. (2020). (**Added:** To derive a probability distribution function for the age of δ Lyr cluster, we then assumed a Gaussian likelihood that treated the interpolated isochrones as the “model” and the δ Lyr cluster’s isochrone as the “data” (Equation 7 from Gagné et al. 2020). The cluster’s age and its statistical uncertainty are then quoted as the the mean and standard deviation of this age posterior.)

The ages returned by this procedure depend on the ages assumed for each reference cluster. We adopted a 115 Myr age for the Pleiades (Dahm 2015), and a 16 Myr age for UCL (Pecaut & Mamajek 2016). The age of IC 2602 however is the most important ingredient, since it receives the most weight in the interpolation. Plausible ages for IC 2602 span 30 Myr to 46 Myr, with older ages being preferred by the lithium-depletion-boundary (LDB) measurements (Dobbie et al. 2010; Randich et al. 2018) and younger ages by the main-sequence turn-off (Stauffer et al. 1997; David & Hillenbrand 2015; Bossini et al. 2019). If we were to adopt the 30 Myr age for IC 2602, then the δ Lyr cluster would be 31^{+5}_{-4} Myr old. For the converse extreme of 46 Myr, the δ Lyr cluster would be 44^{+8}_{-7} Myr old. We adopt an intermediate 38 Myr age for IC 2602, which yields an age for the δ Lyr cluster of 38^{+6}_{-5} Myr.³ Follow-up studies of the LDB or main-sequence turn-off in the δ Lyr cluster could help determine a more precise and accurate age for the cluster, and are left for future work.

² For a description of the renormalized unit weight error (RUWE), see the GAIA DPAC technical note http://www.rssd.esa.int/doc_fetch.php?id=3757412.

³ Our exploration of the PARSEC and MIST isochrone models over a grid of ages, metallicities, and reddening, yielded the best agreement for this ≈ 38 Myr age as well, given $[Fe/H] = +0.1$ and $A_V = 0.2$ (Bressan et al. 2012; Choi et al. 2016); this preferred CAMD reddening is higher than the Lallement et al. (2018) value by a factor of two.

254

2.2.2. Stellar Rotation Periods

255 Of the 3,071 candidate δ Lyr cluster members re-
 256 ported by Kounkel & Covey (2019), 924 stars were
 257 amenable to rotation period measurements ($G < 17$
 258 and $(G_{BP} - G_{RP})_0 > 0.5$) using the TESS full frame
 259 image data. (**Added:** As a matter of scope, we re-
 260 stricted our attention to the 391 stars discussed
 261 in Section 2.1 in the spatial and kinematic prox-
 262 imity of Kepler 1627.) We extracted light curves
 263 from the TESS images using the nearest pixel to
 264 each star, and regressed them against systematics
 265 with the causal pixel model implemented in the
 266 unpopular package (Hattori et al. 2021). We
 267 then measured candidate rotation periods using a
 268 Lomb-Scargle periodogram (Lomb 1976; Scargle
 269 1982; Astropy Collaboration et al. 2018). To en-
 270 able cuts on crowding, we queried the Gaia source
 271 catalog for stars within a $21.^0$ radius of the tar-
 272 get star (a radius of 1 TESS pixel). Within this ra-
 273 dius, we recorded the number of stars with greater
 274 brightness than the target star, and with brightness
 275 within 1.25 TESS magnitudes of the target star.

276 We then cleaned the candidate TESS rotation pe-
 277 riod measurements through a combination of auto-
 278 mated and manual steps. (**Deleted:** As a matter
 279 of scope, we restricted our attention to the 391
 280 stars discussed in Section 2.1 in the spatial and
 281 kinematic proximity of Kepler 1627.) Kepler
 282 rotation periods were derived by McQuillan et al.
 283 (2014) for 28 of (**Replaced:** these replaced with:
 284 our 391)stars; for these cases, we simply adopted
 285 the Kepler rotation period. For the remaining stars
 286 with only TESS data, we focused only on the
 287 stars for which no companions were known with
 288 a brightness exceeding one-tenth of the target star
 289 in a $21.^0$ radius. There were 192 stars that met
 290 these crowding requirements, and that had TESS
 291 data available. For plotting purposes we then im-
 292 posed a selection based on the strength of the sig-
 293 nal itself: we required the Lomb Scargle power to
 294 exceed 0.2, and the period to be below 15 days.

295 The lower panel of Figure 3 shows the result-
 296 ing 145 stars. The majority of these stars fall be-
 297 low the “slow sequence” of the Pleiades, consistent
 298 with a gyrochronal age for the δ Lyr cluster below
 299 100 Myr. In fact, the rotation-color distributions of
 300 other 30 Myr to 50 Myr clusters (e.g., IC 2602 and
 301 IC 2391) are indistinguishable(**Added:** from each
 302 other) (Douglas et al. 2021). Approximately 10 of
 303 the δ Lyr cluster stars appear as outliers above the
 304 “slow sequence”. Assuming that they are all false
 305 positives (*i.e.*, field interlopers), our rotation pe-
 306 riod detection fraction would be $135/192 \approx 70\%$.
 307 (**Replaced:** The other stars are likely to be field
 308 contaminants. replaced with: Although some
 309 of these outlier stars might be unresolved F+K
 310 binaries that are in the cluster (Stauffer et al.

311 **2016), assuming that they are field contaminants provides a more secure lower bound of the**
 312 **rotation period detection fraction.) A final pos-**
 313 **sible confounding factor – binarity – is known to**
 314 **affect the “fast sequence” of stars beneath the slow**
 315 **sequence (Meibom et al. 2007; Gillen et al. 2020;**
 316 **Bouma et al. 2021). We do not expect it to change**
 317 **the central conclusion regarding the cluster’s age.**

319 3. THE STARS
 320 3.1. *Kepler* 1627A
 321 3.1.1. *Age*

322 Based on the spatial and kinematic association of
 323 Kepler 1627 with the δ Lyr cluster, and the assumption
 324 that the planet formed shortly after the star, it
 325 seems likely that Kepler 1627 is the same age as
 326 the cluster. There are two consistency checks on
 327 whether this is true: rotation and lithium. Based
 328 on the Kepler light curve, the rotation period is
 329 2.642 ± 0.042 days, where the quoted uncertainty
 330 is based on the scatter in rotation periods measured
 331 from each individual Kepler quarter. This is consist-
 332 tent with comparable cluster members (Figure 3).

333 To infer the amount of Li I from the 6708 Å dou-
 334 blet (e.g., Soderblom et al. 2014), we acquired
 335 an iodine-free spectrum from Keck/HIRES on the
 336 night of 2021 March 26 using the standard setup
 337 and reduction techniques of the California Planet
 338 Survey (Howard et al. 2010). Following the equiv-
 339 alent width measurement procedure described by
 340 Bouma et al. (2021), we find $\text{EW}_{\text{Li}} = 233^{+5}_{-7}$ mÅ.
 341 This value does not correct for the Fe I blend
 342 at 6707.44Å. Nonetheless, given the stellar effec-
 343 tive temperature (Table 1), this measurement is in
 344 agreement with expectations for a ≈ 40 Myr star
 345 (e.g., as measured in IC 2602 by Randich et al.
 346 2018). It is also larger than any lithium equivalent
 347 widths measured by Berger et al. (2018) in their
 348 analysis of 1,301 Kepler-star spectra.

349 3.1.2. *Stellar Properties*

350 The adopted stellar parameters are listed in Ta-
 351 ble 1. The stellar mass, radius, and effective
 352 temperature are found by interpolating against a
 353 38 Myr MIST isochrone (Choi et al. 2016). The
 354 statistical uncertainties are propagated from the
 355 absolute magnitude (mostly originating from the
 356 parallax uncertainty) and the color; the system-
 357 atic uncertainties are taken to be the difference
 358 between the PARSEC (Bressan et al. 2012) and
 359 MIST isochrones. Reported uncertainties are a
 360 quadrature sum of the statistical and systematic
 361 components. As a consistency check, we ana-
 362 lyzed the aforementioned Keck/HIRES spectrum
 363 from the night of 2021 March 26 using a com-
 364 bination of SpecMatch-Emp for stellar prop-
 365 erties, and SpecMatch-Synth for $v\sin i$ (Yee

366 et al. 2017). This procedure yielded $T_{\text{eff}} = 5498 \pm$
 367 100 K, $\log g = 4.6 \pm 0.1$, $[\text{Fe}/\text{H}] = 0.15 \pm 0.10$ from
 368 SpecMatch-Emp, and $v\sin i = 18.9 \pm 1.0$ from
 369 SpecMatch-Synth. These values are within the
 370 $1-\sigma$ uncertainties of our adopted values from the
 371 isochrone interpolation.

372 3.2. *Kepler* 1627B

373 We first noted the presence of a close neighbor in
 374 the Kepler 1627 system on 2015 July 22 when we
 375 acquired adaptive optics imaging using the NIRC2
 376 imager on Keck-II. We used the narrow camera
 377 ($\text{FOV} = 10.2''$) to obtain 8 images in the K' fil-
 378 ter ($\lambda = 2.12 \mu\text{m}$) with a total exposure time of
 379 160 s. We analyzed these data following Kraus
 380 et al. (2016), which entailed using PSF-fitting to
 381 measure the separation, position angle, and con-
 382 trast of the candidate companion. The best-fitting
 383 empirical PSF template was identified from among
 384 the near-contemporaneous observations of single
 385 stars in the same filter. The mean values inferred
 386 from the 8 images are reported in Table 1. To es-
 387 timate the detection limits, we analyzed the resid-
 388 uals after subtracting the empirical PSF template.
 389 Within each residual image, the flux was measured
 390 through 40 mas apertures centered on every pixel,
 391 and then the noise as a function of radius was esti-
 392 mated from the RMS within concentric rings. Fi-
 393 nally, the detection limits were estimated from the
 394 strehl-weighted sum of the detection significances
 395 in the image stack, and we adopted the $6-\sigma$ thresh-
 396 old as the detection limit for ruling out additional
 397 companions.

398 We also observed Kepler 1627 on Gemini-North
 399 using the ‘Alopeke speckle imager on 2021 June
 400 24. ‘Alopeke is a dual-channel speckle interfer-
 401 ometer that uses narrow-band filters centered at
 402 $0.83 \mu\text{m}$ and $0.56 \mu\text{m}$. We acquired three sets
 403 of 1000×60 msec exposures during good seeing
 404 ($0.45''$), and used the autocorrelation function of
 405 these images to reconstruct a single image and $5-$
 406 σ detection limits (see Howell et al. 2011). This
 407 procedure yielded a detection of the companion in
 408 the $0.83 \mu\text{m}$ notch filter, but not the $0.56 \mu\text{m}$ filter.
 409 The measured projected separation and magnitude
 410 difference are given in Table 1.

411 Figure 4 summarizes the results of the high-
 412 resolution imaging. The Gaia EDR3 parallax for
 413 the primary implies a projected separation of $53 \pm$
 414 4 AU, assuming the companion is bound. Al-
 415 though the companion is unresolved in the Gaia
 416 source catalog (there are no comoving, codistant
 417 candidate companions brighter than $G < 20.5$ mag
 418 within $\rho < 120''$), its existence was also suggested
 419 by the primary star’s large (Replaced: renormal-
 420 ized unit weight error (RUWE), replaced with:
 421 RUWE) relative to other members of the δ Lyr
 422 cluster (Added: (RUWE≈2.9; roughly the 98th

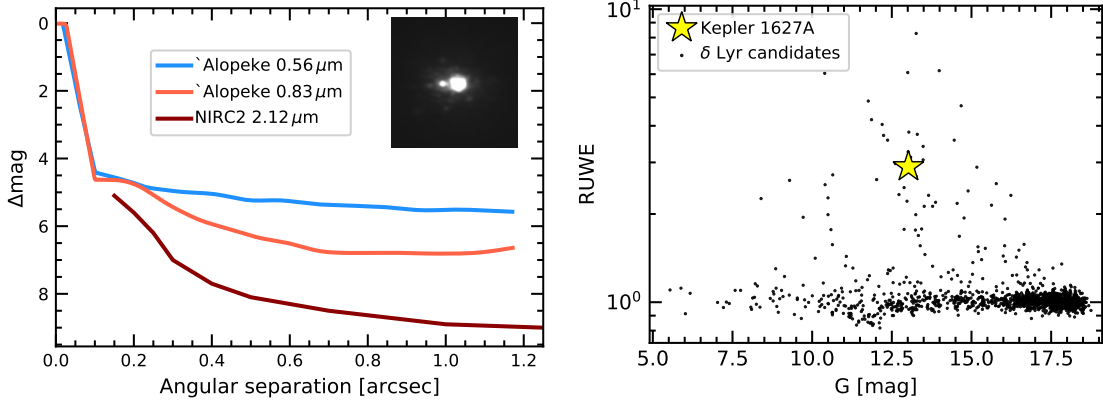


Figure 4. Kepler 1627 is a binary. *Left:* High-resolution imaging from Gemini-North/‘Alopeke and Keck/NIRC2 shows an \approx M2.5V companion at $\rho \approx 0.^{\prime\prime}16$, which corresponds to a projected separation of 53 ± 4 AU. The inset shows a cutout of the stacked NIRC2 image (North is up, East is left, scale is set by the separation of the binary). The lines show $5-\sigma$ contrast limits for the ‘Alopeke filters, and $6-\sigma$ contrast limits for NIRC2 outside of $0.^{\prime\prime}15$. *Right:* Gaia EDR3 renormalized unit weight error (RUWE) point estimates for candidate δ Lyr cluster members. Since other members of the cluster with similar brightnesses have comparable degrees of photometric variability, the high RUWE independently suggests that Kepler 1627 is a binary.

percentile of the cluster’s distribution)). Based on the apparent separation, the binary orbital period is of order hundreds of years. The large RUWE is therefore more likely to be caused by a PSF-mismatch skewing the Gaia centroiding during successive scans, rather than true astrometric motion. Regardless, given the low geometric probability that a companion imaged at $\rho \approx 0.^{\prime\prime}16$ is a chance line-of-sight companion, we proceed under the assumption that the companion is bound, and that Kepler 1627 is a binary. Given the distance and age, the models of Baraffe et al. (2015) imply a companion mass of $M_B \approx 0.33M_{\odot}$ and companion temperature of $T_{\text{eff},B} \approx 3450$ K. The corresponding spectral type is roughly M2.5V (Pecaut & Mamajek 2013). These models combined with the NIRC2 contrast limits imply physical limits on tertiary companions of $M_{\text{ter}} < 50M_{\text{Jup}}$ at $\rho = 50$ AU, $M_{\text{ter}} < 20M_{\text{Jup}}$ at $\rho = 100$ AU, and $M_{\text{ter}} < 10M_{\text{Jup}}$ at $\rho = 330$ AU.

4. THE PLANET

4.1. Kepler Light Curve

The Kepler space telescope observed Kepler 1627 at a 30-minute cadence from 2009 May 2 until 2013 April 8. Data gaps during quarters 4, 9, and 13 led to an average duty cycle over the 3.9 year interval of 67%. Kepler 1627 was also observed at 1-minute cadence from 2012 Oct 5 until 2013 Jan 11. The top panel of Figure 5 shows a portion of the 30-minute cadence PDCSAP light curve. Nonastrophysical variability has been removed using the methods discussed by Smith et al. (2017); the default optimal aperture was assumed (Smith et al. 2016). Cadences with non-zero quality flags (9%

of the data) have been omitted. The resulting photometry is dominated by a quasi-periodic starspot signal with a peak-to-peak amplitude that varies between 2% and 8%. (Added: Given that the secondary companion’s brightness in the Kepler band is \approx 1.5% that of the primary, source confusion for the rotation signal is not expected to be an issue.) Previous analyses have identified and characterized the smaller transit signal (Tenenbaum et al. 2012; Thompson et al. 2018), validated its planetary nature (Morton et al. 2016), and even searched the system for transit timing variations (Holczer et al. 2016). Nonetheless, since the cluster membership provides us with more precise stellar parameters than those previously available, we opted to reanalyze the light curve.

4.1.1. Transit and Stellar Variability Model

We fitted the Kepler long cadence time series with a model that simultaneously included the planetary transit and the stellar variability. The stellar variability was modeled with the RotationTerm Gaussian Process kernel in exoplanet (Foreman-Mackey et al. 2020). This kernel assumes that the variability is generated by a mixture of two damped simple harmonic oscillators with characteristic frequencies set by $1/P_{\text{rot}}$ and its first harmonic. We additionally included a jitter term to inflate the flux uncertainties in a manner that accounted for otherwise unmodeled excess white noise, and let the eccentricity float. For the limb-darkening, we assumed a quadratic law, and sampled using the uninformative prior suggested by Kipping (2013).

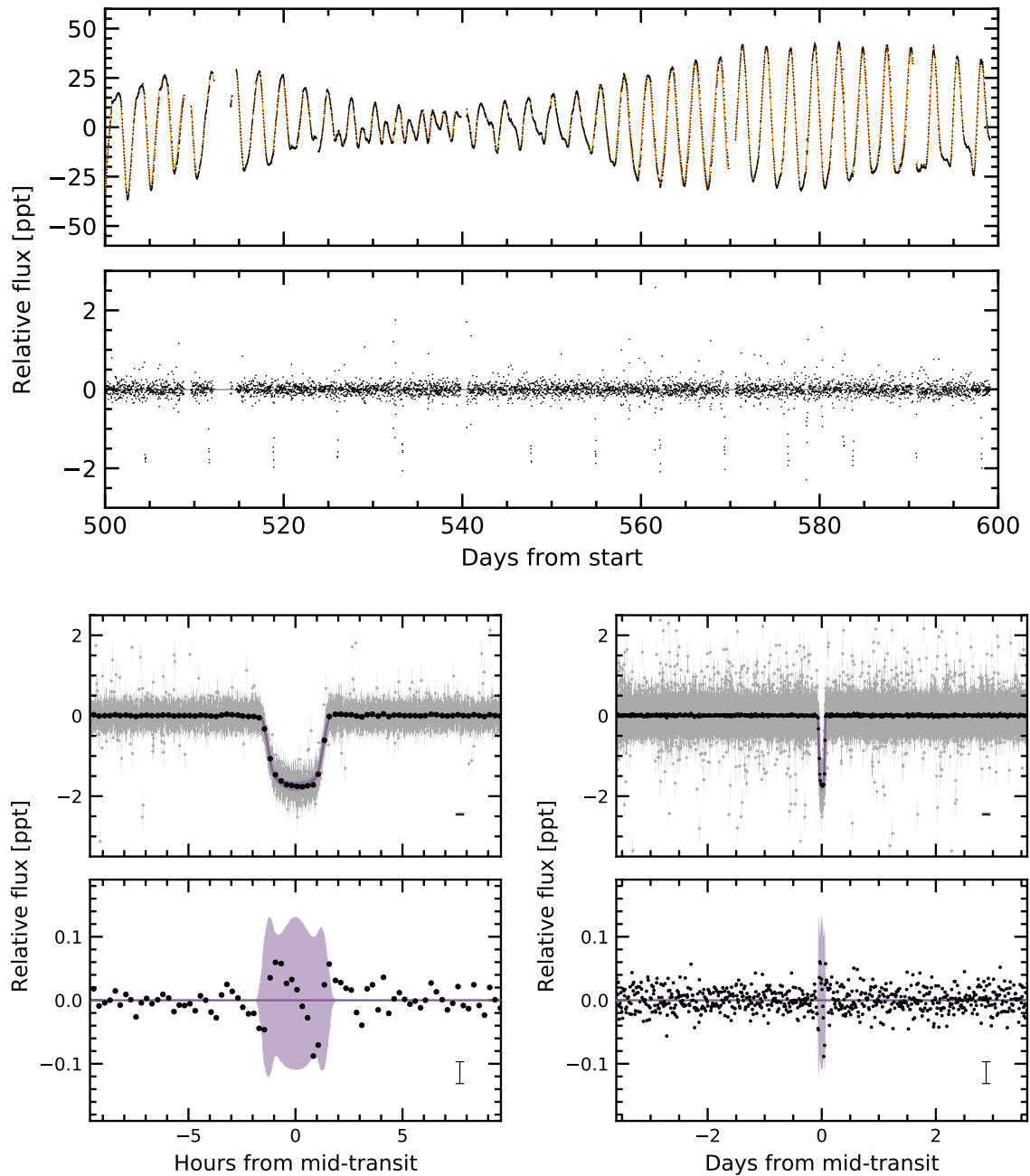


Figure 5. The light curve of Kepler 1627. *Top:* The Kepler data span 1,437 days (3.9 years), sampled at 30 minute cadence; a 100 day segment is shown. The top panel shows the PDCSAP median-subtracted flux in units of parts-per-thousand ($\times 10^{-3}$). The dominant signal is induced by starspots. The stellar variability model (orange line) is subtracted below, revealing the transits of Kepler 1627Ab. The online Figure Set spans the entire 3.9 years of observations. *Bottom:* Phase-folded transit of Kepler 1627Ab with stellar variability removed. Windows over 20 hours (*left*) and the entire orbit (*right*) are shown, and the residual after subtracting the transit is in the bottom-most row. The 2- σ model uncertainties and the best-fit model are the light purple band and the dark purple line. Gray points are individual flux measurements; black points bin these to 15 minute intervals, and have a representative 1- σ error bar in the lower right of each panel. The asymmetric residual during transit is larger than the out-of-transit scatter.

Our model therefore included 10 free parameters for the transit ($\{P, t_0, \delta, b, u_1, u_2, R_\star, \log g, e, \omega\}$), 2 free parameters for the light curve normalization and a white noise jitter ($\{\langle f \rangle, \sigma_f\}$), and 5 hyperparameters for the GP ($\{\sigma_{\text{rot}}, P_{\text{rot}}, Q_0, dQ, f\}$). We also considered including an additive SHOTerm kernel to account for stochastic noise, but found that this did not affect the results, and so opted for the simpler GP kernel. We fitted the models using PyMC3 (Salvatier et al. 2016; Theano Development Team 2016), and accounted for the finite integration time of each exposure in the numerical integration when evaluating the model light curve (see Kipping 2010). We assumed a Gaussian likelihood, and after initializing each model with the parameters of the maximum *a posteriori* model, we sampled using PyMC3’s gradient-based No-U-Turn Sampler (Hoffman & Gelman 2014) in the bases indicated in Table 2. We used \hat{R} as our convergence diagnostic (Gelman & Rubin 1992).

Figure 5 shows the resulting best-fit model in orange (top) and purple (bottom). The model parameters and their uncertainties, given in Table 2, are broadly consistent with a mini-Neptune sized planet ($3.82 \pm 0.16 R_\oplus$) on a close-in circular⁴ orbit around a G8V host star ($0.88 \pm 0.02 R_\odot$). This best-fit planet size is consistent with those previously reported by Morton et al. (2016) and Berger et al. (2018), and corrects for the small amount of flux dilution from Kepler 1627B.

4.1.2. Transit Asymmetry

The transit fit however is not perfect: the lower panels of Figure 5 show an asymmetric residual in the data relative to the model: the measured flux is high during the first half of transit, and low in the second half. The semi-amplitude of this deviation is ≈ 50 ppm, which represents a $\approx 3\%$ distortion of the transit depth ($\delta = 1759 \pm 62$ ppm). Note that although this asymmetry is within the 2σ model uncertainties, the model has a jitter term that grows to account for excess white noise in the flux. The significance of the asymmetry is therefore best assessed in comparison against the intrinsic out-of-transit scatter in the data (≈ 16 ppm), not the model uncertainties. The lower right panel of Figure 5 demonstrates that the scatter during transit is higher than during all other phases of the planet’s orbit.

To determine whether the asymmetry could be a systematic caused by our stellar variability model, we explored an alternative approach in which we isolated each transit window, locally fitted out polynomial trends, and then binned all the ob-

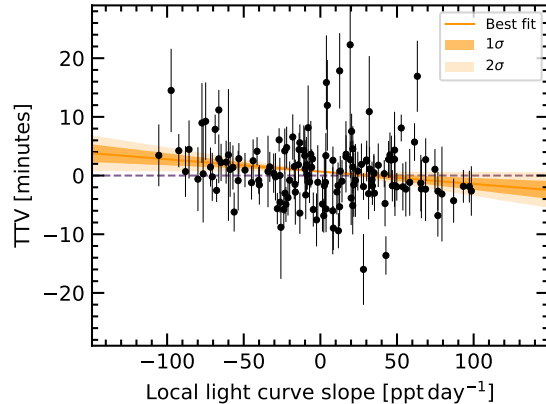


Figure 6. Possible evidence for a prograde orbit of Kepler 1627 Ab. The time of each Kepler transit was measured, along with the local slope of the light curve. The two quantities are weakly anti-correlated ($\approx 2\sigma$), which might be caused by starspot crossings during the first (second) half of transit inducing a positive (negative) TTV, provided that the orbit is prograde (Mazeh et al. 2015). The units along the abscissa can be understood by considering that the stellar flux changes by ~ 60 ppt per half rotation period (~ 1.3 days).

served transits; the asymmetry was still present at a comparable amplitude. Appendix B describes a more detailed analysis, which finds that the asymmetry also seems to be robust to different methods of data binning in time and by local light curve slope. Possible astrophysical explanations are discussed in Section 5.

4.1.3. Transit Timing and the Local Slope

The previous analysis by Holczer et al. (2016) did not find any significant long-term transit timing or duration variations (TTVs or TDVs) for Kepler 1627. Quantitatively, the mean and standard deviation of the TTVs and TDVs they measured were -1.1 ± 13.8 min and -3.3 ± 22.1 min. In an earlier analysis however, Holczer et al. (2015) studied correlations between TTVs and local light curve slopes, and for Kepler 1627 found a weak correlation of -29 ± 13 min day $^{-1}$ between the two quantities. Given the possible connection between such correlations and the unresolved starspot crossings that we expect to be present in the Kepler 1627 light curve (Mazeh et al. 2015), we opted to re-examine the individual transit times.

We therefore isolated each of the 144 observed transits to within ± 4.5 hr of each transit, and fitted each window with both *i*) a local polynomial baseline plus the transit, and *ii*) a local linear trend. We considered the results both for a second and fourth-order time-dependence in the local baseline. We let the mid-time of each transit float, and then calculated the residual between the measured mid-time

⁴ Our transit fitting yields $e < 0.48$ at 2σ ; the constraints on the eccentricity are not particularly strong.

and that of a periodic orbit. This residual, the transit timing variation, is plotted in Figure 6 against the local linear slope for the fourth-order polynomial baseline. The slope of $-21 \pm 10 \text{ min day}^{-1}$ is similar to that found by Holczer et al. (2015).

One concern we had in this analysis was whether our transit fitting procedure might induce spurious correlations between the slope and transit time. In particular, using the second-order polynomial baseline yielded a larger anti-correlation between the TTVs and local slopes, of $-79 \pm 14 \text{ min day}^{-1}$. We therefore performed an injection-recovery procedure in which we injected transits at different phases in the Kepler 1627 light curve and repeated the TTV analysis. This was done at ≈ 50 phases, each separated by $0.02 P_{\text{orb}}$ while omitting the phases in transit. For the second-order polynomial baseline, this procedure yielded a similar anti-correlation in the injected transits as that present in the real transit; using this baseline would therefore bias the result. However for the fourth-order baseline, the correlation present in the data was stronger than in all but one of the injected transits. Possible interpretations are discussed below. Given the statistical significance, this analysis should be interpreted as suggestive at best.

4.2. Planet Confirmation

If the Kepler 1627Ab transit signal is created by a genuine planet, then to our knowledge it would be the youngest planet yet found by the main Kepler mission.⁵ Could the transit be produced by anything other than a planet orbiting this near-solar analog? Morton et al. (2016) validated the planet based on the transit shape, arguing that the most probable false positive scenario was that of a background eclipsing binary, which had a model-dependent probability of $\approx 10^{-5}$. However, this calculation was performed without knowledge of the low-mass stellar companion ($M_B \approx 0.33 M_{\odot}$). Validated planets have also previously been refuted (e.g., Shporer et al. 2017). We therefore reassessed false positive scenarios in some detail.

As an initial plausibility check, Kepler 1627B contributes 1% to 2% of the total flux observed in the Kepler aperture. For the sake of argument, assume the former value. The observed transit has a depth of $\approx 0.18\%$. A 18% deep eclipse of Kepler 1627B would therefore be needed to produce a signal with the appropriate depth. The shape of the transit signal however requires the impact parameter to be below 0.77 (2- σ); the tertiary transit-

⁵ The re-purposed K2 mission however has found two younger systems containing five planets: K2-33b ($9 \pm 1 \text{ Myr}$; Mann et al. 2016; David et al. 2016) and V1298 Tau ($23 \pm 4 \text{ Myr}$; David et al. 2019).

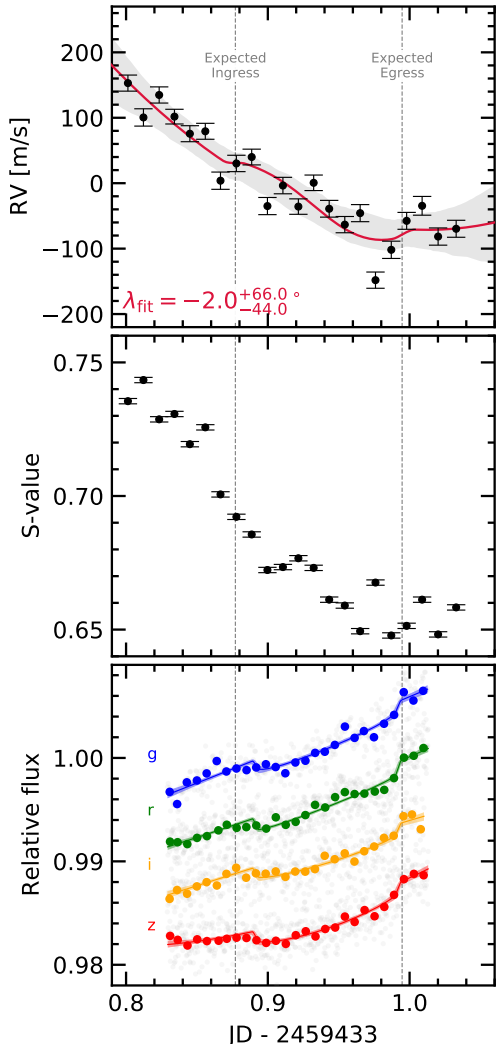


Figure 7. Keck/HIRES radial velocities and MuSCAT3 photometry from the transit of 2021 Aug 7. Top: The radial velocity jitter across the 15 minute exposures ($\sigma_{\text{RV}} \approx 30 \text{ m s}^{-1}$) prevented us from detecting the RM effect; a model including the RM anomaly and a quadratic trend in time to fit the spot-induced $\approx 250 \text{ m s}^{-1}$ trend is shown (see Appendix C). Shaded bands show $2-\sigma$ model uncertainties. Middle: The RV variations are strongly correlated with varying emission in the Ca H and K lines. Bottom: The photometric transit depths are consistent across the *griz* bandpasses. The photometry is binned at 10 minute intervals.

ing the secondary would therefore need to be non-grazing with $R_3/R_2 \approx 0.4$. This yields a contradiction: this scenario requires an ingress and egress phase that each span $\approx 40\%$ of the transit duration ($\approx 68 \text{ min}$). The actual measured ingress and egress duration is $\approx 17 \text{ min}$, a factor of four times too short. The combination of Kepler 1627B's brightness, the transit depth, and the ingress du-

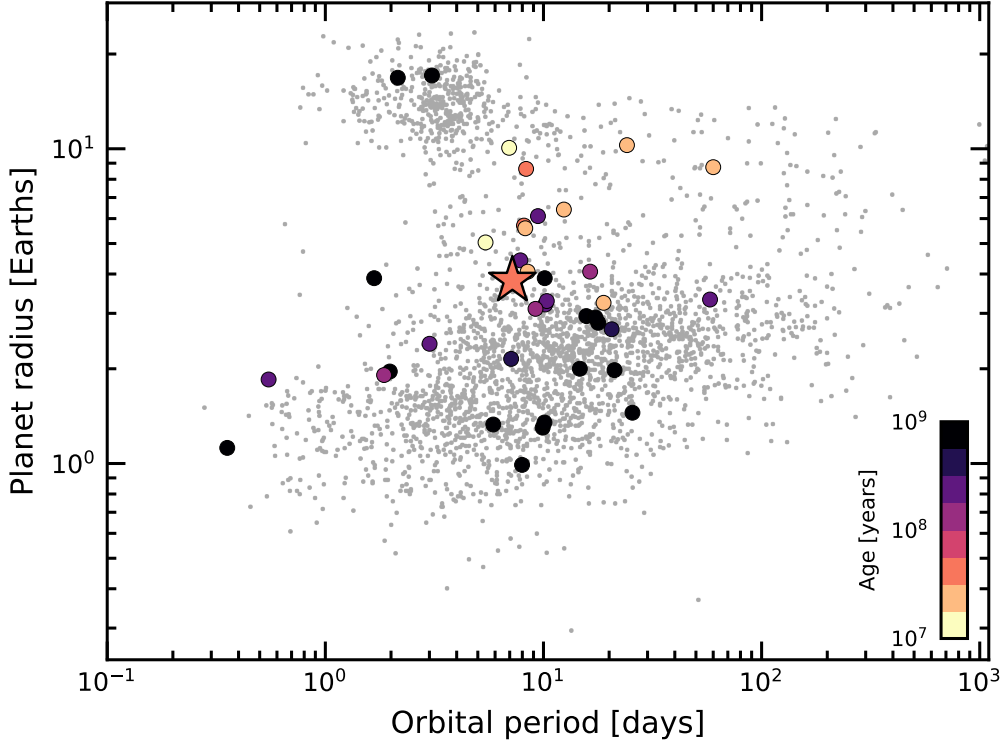


Figure 8. Radii, orbital periods, and ages of transiting exoplanets. Planets younger than a gigayear with $\tau/\sigma_\tau > 3$ are emphasized, where τ is the age and σ_τ is its uncertainty. Kepler 1627Ab is shown with a star. The large sizes of the youngest transiting planets could be explained by their primordial atmospheres not yet having evaporated; direct measurements of the atmospheric outflows or planetary masses would help to confirm this expectation. Selection effects may also be important. Parameters are from the NASA Exoplanet Archive (2021 Sept 15).

ration therefore disfavor the scenario that Kepler 1627B might host the transit signal.

Beyond this simple test, a line of evidence that effectively confirms the planetary interpretation is that the stellar density implied by the transit duration and orbital period is inconsistent with an eclipsing body around the M-dwarf companion. We find $\rho_* = 2.00 \pm 0.24 \text{ g cm}^{-3}$, while the theoretically expected density for Kepler 1627B is $\approx 4.6 \text{ g cm}^{-3}$ (Table 2; Choi et al. 2016). The transit duration is therefore too long to be explained by a star eclipsing the M dwarf secondary at 10σ . While the planet might hypothetically still orbit a hidden close and bright companion, this possibility is implausible given *i*) the lack of secondary lines in the HIRES spectra, *ii*) the lack of secondary rotation signals in the Kepler photometry, and *iii*) the proximity of Kepler 1627 to the δ Lyr cluster locus on the Gaia CAMD (Figure 3).

The correlation noted in Section 4.1.3 between the TTVs and the local light curve slope might be an additional line of evidence in support of the planetary interpretation. Unless it is a statistical fluke (a $\approx 5\%$ possibility), then the most likely cause of the correlation is unresolved starspot crossings (Mazeh et al. 2015). These would only

be possible if the planet transits the primary star, which excludes a background eclipsing binary scenario. The correlation would also suggest that the planet's orbit is prograde. The latter point assumes that the dominant photometric variability is induced by dark spots, and not bright faculae. Given the observed transition of Sun-like stellar variability from spot to faculae-dominated regimes between young and old ages, we expect this latter assumption to be reasonably secure (Shapiro et al. 2016; Montet et al. 2017; Reinhold & Hekker 2020).

A third supporting line of evidence for the planetary interpretation also exists. We observed a transit of Kepler 1627Ab on the night of 2021 Aug 7 simultaneously with Keck/HIRES and MuSCAT3. We scheduled the observations using the ephemeris of Holczer et al. (2016). Although we did not detect the Rossiter-McLaughlin (RM) anomaly, the multi-band MuSCAT3 light curves show that the transit is achromatic (Figure 7). Quantitatively, when we fitted the MuSCAT3 photometry with a model that lets the transit depths vary across each bandpass, we found *griz* depths consistent with the Kepler depth at 0.6, 0.3, 0.3, and 1.1σ respectively. Conditioned on the ephemeris and transit

depth from the Kepler data, the MuSCAT3 observations also suggested a transit duration 17.3 ± 4.3 min shorter than the Kepler transits. However, given both the lack of TDVs in the Kepler data and the relatively low signal-to-noise of the MuSCAT3 transit, further photometric follow-up would be necessary to determine whether the transit duration is indeed changing. For our RM analysis, the details are discussed in Appendix C. While the velocities are marginally more consistent with a prograde or polar orbit than a retrograde orbit, the spot-corrected exposure-to-exposure scatter ($\sigma_{RV} \approx 30 \text{ m s}^{-1}$) is comparable to the expected RM anomaly assuming an aligned orbit ($\Delta v_{RM} \approx 20 \text{ m s}^{-1}$). We are therefore not in a position to claim a spectroscopic detection of the RM effect, nor to quantify the stellar obliquity.

5. DISCUSSION & CONCLUSIONS

Kepler 1627Ab provides a new extremum in the ages of the Kepler planets, and opens multiple avenues for further study. Observations of spectroscopic transits at greater precision should yield a measurement of the stellar obliquity, which would confirm or refute the prograde orbital geometry suggested by the TTV-local slope correlation. Separately, transit spectroscopy aimed at detecting atmospheric outflows could yield insight into the evolutionary state of the atmosphere (e.g., Ehrenreich et al. 2015; Spake et al. 2018; Vissapragada et al. 2020). Observations that quantify the amount of high-energy irradiation incident on the planet would complement these efforts, by helping to clarify the expected outflow rate (e.g., Poppenhaeger et al. 2021). Finally, a challenging but informative quantity to measure would be the planet’s mass. Measured at sufficient precision, for instance through a multi-wavelength radial velocity campaign, the combination of the size, mass, and age would yield constraints on both the planet’s composition and its initial entropy (Owen 2020).

More immediately, the Kepler data may yet contain additional information. For instance, one possible explanation for the transit asymmetry shown in Figure 5 is that of a dusty asymmetric outflow. Dusty outflows are theoretically expected for young mini-Neptunes, and the amplitude of the observed asymmetry is consistent with predictions (Wang & Dai 2019). A second possibility is that the planetary orbit is slightly misaligned from the stellar spin axis, and tends to transit starspot groups at favored stellar latitudes. This geometry would be necessary in order to explain how the starspot crossings could add up coherently. Other possibilities including gravity darkening or TTVs causing the asymmetry are disfavored (see Appendix B).

Beyond the asymmetric transits, Appendix D highlights an additional abnormality in the short-

cadence Kepler data, in the arrival time distribution of stellar flares. We encourage its exploration by investigators more versed in the topic than ourselves.

In the context of the transiting planet population, Kepler 1627Ab is among the youngest known (Figure 8). Comparable systems with precise ages include K2-33 (Mann et al. 2016; David et al. 2016), DS Tuc (Benatti et al. 2019; Newton et al. 2019), HIP 67522 (Rizzuto et al. 2020), TOI 837 (Bouma et al. 2020), the two-planet AU Mic (Plavchan et al. 2020; Martioli et al. 2021) and the four-planet V1298 Tau (David et al. 2019). Kepler 1627Ab is one of the smaller planets in this sample ($3.82 \pm 0.16 R_\oplus$), which could be linked to the selection effects imposed by spot-induced photometric variability at very young ages (e.g., Zhou et al. 2021). However, smaller planets could have been detected: the Kepler pipeline’s median completeness extended to $1.6 R_\oplus$ at 10 day orbital periods, and $3.3 R_\oplus$ at 100 days (Burke & Catanzarite 2021). The large size of Kepler 1627Ab relative to most Kepler mini-Neptunes might therefore support a picture in which the typical $5 M_\oplus$ to $10 M_\oplus$ mini-Neptune (Wu 2019) loses a significant fraction of its primordial atmosphere over its first gigayear (Owen & Wu 2013; Ginzburg et al. 2018).

Ultimately, the main advance of this work is a precise measurement of the age of Kepler 1627Ab. This measurement was enabled by identifying the connection of the star to the δ Lyr cluster using Gaia kinematics, and by then using the Gaia color-absolute magnitude diagram and TESS stellar rotation periods to verify the cluster’s existence. Table 3 enables similar cross-matches for both known and forthcoming exoplanet systems (e.g., Guerrero et al. 2021). Confirming these candidate associations using independent age indicators is essential because their false positive rates are not known. A related path is to identify new kinematic associations around known exoplanet host stars using positions and tangential velocities from Gaia, and to verify these associations with stellar rotation periods and spectroscopy (e.g., Tofflemire et al. 2021). Each approach seems likely to expand the census of planets with precisely measured ages over the coming years, which will help in deciphering the early stages of exoplanet evolution.

ACKNOWLEDGMENTS

The authors are grateful to J. Winn, J. Spake, A. Howard, and T. David for illuminating discussions and suggestions, and to R. Kerr for providing us with the Kerr et al. (2021) membership list prior to its publication. The authors are

795 also grateful to K. Collins for helping resolve the
 796 scheduling conflict that would have otherwise pre-
 797 vented the MuSCAT3 observations. L.G.B. ac-
 798 knowledges support from a Charlotte Elizabeth
 799 Procter Fellowship from Princeton University, as
 800 well as from the TESS GI Program (NASA grants
 801 80NSSC19K0386 and 80NSSC19K1728) and the
 802 Heising-Simons Foundation (51 Pegasi b Fellow-
 803 ship). Keck/NIRC2 imaging was acquired by pro-
 804 gram 2015A/N301N2L (PI: A. Kraus). In addition,
 805 this paper is based in part on observations made
 806 with the MuSCAT3 instrument, developed by the
 807 Astrobiology Center and under financial support by
 808 JSPS KAKENHI (JP18H05439) and JST PRESTO
 809 (JPMJPR1775), at Faulkes Telescope North on
 810 Maui, HI, operated by the Las Cumbres Observa-
 811 tory. This work is partly supported by JSPS KAK-
 812 ENHI Grant Numbers 22000005, JP15H02063,
 813 JP17H04574, JP18H05439, JP18H05442, JST
 814 PRESTO Grant Number JPMJPR1775, the Astro-
 815 biology Center of National Institutes of Natural
 816 Sciences (NINS) (Grant Number AB031010). This
 817 paper also includes data collected by the TESS
 818 mission, which are publicly available from the
 819 Mikulski Archive for Space Telescopes (MAST).
 820 Funding for the TESS mission is provided by
 821 NASA's Science Mission directorate. We thank
 822 the TESS Architects (G. Ricker, R. Vanderspek,
 823 D. Latham, S. Seager, J. Jenkins) and the many
 824 TESS team members for their efforts to make the
 825 mission a continued success. Finally, this research
 826 has made use of the Keck Observatory Archive
 827 (KOA), which is operated by the W. M. Keck Ob-
 828 servatory and the NASA Exoplanet Science Insti-
 829 tute (NExSci), under contract with the National
 830 Aeronautics and Space Administration. We also
 831 thank the Keck Observatory staff for their support
 832 of HIRES and remote observing. We recognize
 833 the importance that the summit of Maunakea has
 834 within the indigenous Hawaiian community, and
 835 are deeply grateful to have the opportunity to con-
 836 duct observations from this mountain.

837 *Software:* altaipony (Ilin et al. 2021),
 838 astrobase (Bhatti et al. 2018), astropy (As-
 839 tropy Collaboration et al. 2018), astroquery
 840 (Ginsburg et al. 2018), corner (Foreman-Mackey
 841 2016), exoplanet (Foreman-Mackey et al.
 842 2020), and its dependencies (Agol et al. 2020; Kip-
 843 ping 2013; Luger et al. 2019; Theano Develop-
 844 ment Team 2016), PyMC3 (Salvatier et al. 2016),
 845 scipy (Jones et al. 2001), TESS-point (Burke
 846 et al. 2020), wotan (Hippke et al. 2019).

847 *Facilities:* Astrometry: Gaia (Gaia Col-
 848 laboration et al. 2018b, 2021a). Imaging:
 849 Second Generation Digitized Sky Survey.
 850 Keck:II (NIRC2; www2.keck.hawaii.edu/inst/

851 nirc2). Gemini:North ('Alopeke; Scott et al. 2018,
 852 2021. Spectroscopy: Keck:I (HIRES; Vogt et al.
 853 1994). Photometry: Kepler (Borucki et al. 2010),
 854 MuSCAT3 (Narita et al. 2020), TESS (Ricker et al.
 855 2015).

Table 1. Literature and Measured Properties for Kepler 1627

| Primary Star | | | |
|---|--|---------------------------------|---------|
| TIC 120105470 GAIADR2 [†] 2103737241426734336 | | | |
| Parameter | Description | Value | Source |
| $\alpha_{J2015.5}$ | Right Ascension (hh:mm:ss) | 18:56:13.6 | 1 |
| $\delta_{J2015.5}$ | Declination (dd:mm:ss) | +41:34:36.22 | 1 |
| V | Johnson V mag. | 13.11 \pm 0.08 | 2 |
| G | Gaia G mag. | 13.02 \pm 0.02 | 1 |
| G_{BP} | Gaia BP mag. | 13.43 \pm 0.02 | 1 |
| G_{RP} | Gaia RP mag. | 12.44 \pm 0.02 | 1 |
| T | TESS T mag. | 12.53 \pm 0.02 | 2 |
| J | 2MASS J mag. | 11.69 \pm 0.02 | 3 |
| H | 2MASS H mag. | 11.30 \pm 0.02 | 3 |
| K _S | 2MASS K _S mag. | 11.19 \pm 0.02 | 3 |
| π | Gaia EDR3 parallax (mas) | 3.009 \pm 0.032 | 1 |
| d | Distance (pc) | 329.5 \pm 3.5 | 1, 4 |
| μ_α | Gaia EDR3 proper motion | 1.716 \pm 0.034 | 1 |
| | in RA (mas yr ⁻¹) | | |
| μ_δ | Gaia EDR3 proper motion | -1.315 \pm 0.034 | 1 |
| | in DEC (mas yr ⁻¹) | | |
| RUWE | Gaia EDR3 renormalized | 2.899 | 1 |
| | unit weight error | | |
| RV | Systemic radial velocity (km s ⁻¹) | -16.7 \pm 1.0 | 5 |
| Spec. Type | Spectral Type | G8V | 5 |
| $v \sin i_*$ | Rotational velocity* (km s ⁻¹) | 18.9 \pm 1.0 | 5 |
| Li EW | 6708Å Equiv. Width (mÅ) | 235 ⁺⁵ ₋₇ | 5 |
| T_{eff} | Effective Temperature (K) | 5505 \pm 60 | 6 |
| $\log g_*$ | Surface Gravity (cgs) | 4.53 \pm 0.05 | 6 |
| R_* | Stellar radius (R_\odot) | 0.881 \pm 0.018 | 6 |
| M_* | Stellar mass (R_\odot) | 0.953 \pm 0.019 | 6 |
| Av | Interstellar reddening (mag) | 0.2 \pm 0.1 | 6 |
| [Fe/H] | Metallicity | 0.1 \pm 0.1 | 6 |
| P_{rot} | Rotation period (d) | 2.642 \pm 0.042 | 7 |
| Age | Adopted stellar age (Myr) | 38 ⁺⁶ ₋₅ | 8 |
| Δm_{832} | Mag difference ('Alopeke 832 nm) | 3.14 \pm 0.15 | 9 |
| θ_B | Position angle (deg) | 92 \pm 1 | 9 |
| ρ_B | Apparent separation of | 0.164 \pm 0.002 | 9 |
| | primary and secondary (as) | | |
| ρ_B | Apparent separation of | 53 \pm 4 | 1, 4, 9 |
| | primary and secondary (AU) | | |
| $\Delta m_{K'}$ | Mag difference (NIRC2 K') | 2.37 \pm 0.02 | 10 |
| θ_B | Position angle (deg) | 95.9 \pm 0.5 | 10 |
| ρ_B | Apparent separation of | 0.1739 \pm 0.0010 | 10 |
| | primary and secondary (as) | | |

NOTE—[†] The GAIADR2 and GAIAEDR3 identifiers for Kepler 1627A are identical. The secondary is not resolved in the Gaia point source catalog. * Given only $v \sin i$ and $2\pi R_*/P_{\text{rot}}$, $\cos i = 0.11^{+0.11}_{-0.08}$. Provenances are: ¹Gaia Collaboration et al. (2021a), ²Stassun et al. (2019), ³Skrutskie et al. (2006), ⁴Lindgren et al. (2021), ⁵HIRESS spectra and Yee et al. (2017), ⁶Cluster isochrone (MIST adopted; PARSEC compared for quoted uncertainty), ⁷Kepler light curve, ⁸Pre-main-sequence CAMD interpolation (Section 2.2.1), ⁹'Alopeke imaging 2021 June 24 (Scott et al. 2021), ¹⁰NIRC2 imaging 2015 July 22, using the Yelda et al. (2010) optical distortion solution to convert pixel-space relative positions to on-sky relative astrometry. The “discrepancy” between the two imaging epochs likely indicates orbital motion.

Table 2. Priors and Posteriors for Model Fitted to the Long Cadence Kepler 1627Ab Light Curve.

| Param. | Unit | Prior | Median | Mean | Std. Dev. | 3% | 97% | ESS | $\hat{R} - 1$ |
|-----------------------|--------------------|---|-------------|-------------|-----------|-------------|-------------|------|---------------|
| <i>Sampled</i> | | | | | | | | | |
| P | d | $\mathcal{N}(7.20281; 0.01000)$ | 7.2028038 | 7.2028038 | 0.0000073 | 7.2027895 | 7.2028168 | 7464 | 3.9e-04 |
| $t_0^{(1)}$ | d | $\mathcal{N}(120.79053; 0.02000)$ | 120.7904317 | 120.7904254 | 0.0009570 | 120.7886377 | 120.7921911 | 3880 | 2.0e-03 |
| $\log \delta$ | — | $\mathcal{N}(-6.3200; 2.0000)$ | -6.3430 | -6.3434 | 0.0354 | -6.4094 | -6.2767 | 6457 | 3.0e-04 |
| $b^{(2)}$ | — | $\mathcal{U}(0.000; 1.000)$ | 0.4669 | 0.4442 | 0.2025 | 0.0662 | 0.8133 | 1154 | 1.6e-03 |
| u_1 | — | Kipping (2013) | 0.271 | 0.294 | 0.190 | 0.000 | 0.628 | 3604 | 1.5e-03 |
| u_2 | — | Kipping (2013) | 0.414 | 0.377 | 0.326 | -0.240 | 0.902 | 3209 | 1.4e-03 |
| R_* | R_{\odot} | $\mathcal{N}(0.881; 0.018)$ | 0.881 | 0.881 | 0.018 | 0.847 | 0.915 | 8977 | 3.1e-04 |
| $\log g$ | cgs | $\mathcal{N}(4.530; 0.050)$ | 4.532 | 4.533 | 0.051 | 4.435 | 4.627 | 6844 | 1.6e-03 |
| $\langle f \rangle$ | — | $\mathcal{N}(0.000; 0.100)$ | -0.0003 | -0.0003 | 0.0001 | -0.0005 | -0.0000 | 8328 | 1.1e-03 |
| $e^{(3)}$ | — | Van Eylen et al. (2019) | 0.154 | 0.186 | 0.152 | 0.000 | 0.459 | 1867 | 2.0e-03 |
| ω | rad | $\mathcal{U}(0.000; 6.283)$ | 0.055 | 0.029 | 1.845 | -3.139 | 2.850 | 3557 | 8.6e-05 |
| $\log \sigma_f$ | — | $\mathcal{N}(\log \langle \sigma_f \rangle; 2.000)$ | -8.035 | -8.035 | 0.008 | -8.049 | -8.021 | 9590 | 3.9e-04 |
| σ_{rot} | d^{-1} | InvGamma(1.000; 5.000) | 0.070 | 0.070 | 0.001 | 0.068 | 0.072 | 9419 | 1.4e-03 |
| $\log P_{\text{rot}}$ | log(d) | $\mathcal{N}(0.958; 0.020)$ | 0.978 | 0.978 | 0.001 | 0.975 | 0.980 | 8320 | 2.2e-04 |
| $\log Q_0$ | — | $\mathcal{N}(0.000; 2.000)$ | -0.327 | -0.326 | 0.043 | -0.407 | -0.246 | 9659 | 2.7e-04 |
| $\log dQ$ | — | $\mathcal{N}(0.000; 2.000)$ | 7.697 | 7.698 | 0.103 | 7.511 | 7.899 | 5824 | 3.7e-04 |
| f | — | $\mathcal{U}(0.010; 1.000)$ | 0.01006 | 0.01009 | 0.00009 | 0.01000 | 0.01025 | 4645 | 4.0e-04 |
| <i>Derived</i> | | | | | | | | | |
| δ | — | — | 0.001759 | 0.001759 | 0.000062 | 0.001641 | 0.001875 | 6457 | 3.0e-04 |
| R_p/R_* | — | — | 0.039 | 0.039 | 0.001 | 0.037 | 0.042 | 1811 | 1.1e-03 |
| ρ_* | g cm^{-3} | — | 1.990 | 2.004 | 0.240 | 1.570 | 2.461 | 6905 | 2.1e-03 |
| $R_p^{(4)}$ | R_{Jup} | — | 0.337 | 0.338 | 0.014 | 0.314 | 0.367 | 2311 | 1.0e-03 |
| $R_p^{(4)}$ | R_{Earth} | — | 3.777 | 3.789 | 0.157 | 3.52 | 4.114 | 2311 | 1.0e-03 |
| a/R_* | — | — | 17.606 | 17.619 | 0.702 | 16.277 | 18.906 | 6905 | 2.1e-03 |
| $\cos i$ | — | — | 0.027 | 0.025 | 0.010 | 0.004 | 0.040 | 1312 | 1.2e-03 |
| T_{14} | hr | — | 2.841 | 2.843 | 0.060 | 2.734 | 2.958 | 3199 | 3.6e-04 |
| T_{13} | hr | — | 2.555 | 2.539 | 0.094 | 2.360 | 2.692 | 1960 | 1.4e-03 |

NOTE— ESS refers to the number of effective samples. \hat{R} is the Gelman-Rubin convergence diagnostic. Logarithms in this table are base-e. \mathcal{U} denotes a uniform distribution, and \mathcal{N} a normal distribution. (1) The ephemeris is in units of BJDTDB - 2454833. (2) Although $\mathcal{U}(0, 1 + R_p/R_*)$ is formally correct, for this model we assumed a non-grazing transit to enable sampling in $\log \delta$. (3) The eccentricity vectors are sampled in the $(e \cos \omega, e \sin \omega)$ plane. (4) The true planet size is a factor of $((F_1 + F_2)/F_1)^{1/2}$ larger than that from the fit because of dilution from Kepler 1627B, where F_1 is the flux from the primary, and F_2 is that from the secondary; the mean and standard deviation of $R_p = 3.817 \pm 0.158 R_{\oplus}$ quoted in the text includes this correction, assuming $(F_1 + F_2)/F_1 \approx 1.015$.

Table 3. Young, Age-dated, and Age-dateable Stars Within the Nearest Few Kiloparsecs.

| Parameter | Example Value | Description |
|-------------------|--|--|
| source_id | 1709456705329541504 | Gaia DR2 source identifier. |
| ra | 247.826 | Gaia DR2 right ascension [deg]. |
| dec | 79.789 | Gaia DR2 declination [deg]. |
| parallax | 35.345 | Gaia DR2 parallax [mas]. |
| parallax_error | 0.028 | Gaia DR2 parallax uncertainty [mas]. |
| pmra | 94.884 | Gaia DR2 proper motion $\mu_{\alpha} \cos \delta$ [mas yr $^{-1}$]. |
| pmdec | -86.971 | Gaia DR2 proper motion μ_{δ} [mas yr $^{-1}$]. |
| phot_g_mean_mag | 6.85 | Gaia DR2 G magnitude. |
| phot_bp_mean_mag | 6.409 | Gaia DR2 G_{BP} magnitude. |
| phot_rp_mean_mag | 7.189 | Gaia DR2 G_{RP} magnitude. |
| cluster | NASAExoArchive_ps_20210506.Uma,IR_excess | Comma-separated cluster or group name. |
| age | 9.48,nan,nan | Comma-separated logarithm (base-10) of reported ^a age in years. |
| mean_age | 9.48 | Mean (ignoring NaNs) of age column. |
| reference_id | NASAExoArchive_ps_20210506,Ujjwal2020,CottenSong2016 | Comma-separated provenance of group membership. |
| reference_bibcode | 2013PASP..125..989A,2020AJ....159..166U,2016ApJS..225..15C | ADS bibcode corresponding to reference_id. |

NOTE— Table 3 is published in its entirety in a machine-readable format. This table is a concatenation of the studies listed in Table 4. One entry is shown for guidance regarding form and content. In this particular example, the star has a cold Jupiter on a 16 year orbit, HD 150706b (Boisse et al. 2012). An infrared excess has been reported (Cotten & Song 2016), and the star was identified by Ujjwal et al. (2020) as a candidate UMa moving group member (≈ 400 Myr; Mann et al. 2020). The star's RV activity and TESS rotation period corroborate its youth.

Table 4. Provenances of Young and Age-dateable Stars.

| Reference | N_{Gaia} | N_{Age} | $N_{G_{\text{RP}} < 16}$ |
|--|-------------------|------------------|--------------------------|
| Kounkel et al. (2020) | 987376 | 987376 | 775363 |
| Cantat-Gaudin & Anders (2020) | 433669 | 412671 | 269566 |
| Cantat-Gaudin et al. (2018) | 399654 | 381837 | 246067 |
| Kounkel & Covey (2019) | 288370 | 288370 | 229506 |
| Cantat-Gaudin et al. (2020) | 233369 | 227370 | 183974 |
| Zari et al. (2018) UMS | 86102 | 0 | 86102 |
| Wenger et al. (2000) Y*? | 61432 | 0 | 45076 |
| Zari et al. (2018) PMS | 43719 | 0 | 38435 |
| Gaia Collaboration et al. (2018a) $d > 250 \text{ pc}$ | 35506 | 31182 | 18830 |
| Castro-Ginard et al. (2020) | 33635 | 24834 | 31662 |
| Kerr et al. (2021) | 30518 | 25324 | 27307 |
| Wenger et al. (2000) Y*○ | 28406 | 0 | 16205 |
| Villa Vélez et al. (2018) | 14459 | 14459 | 13866 |
| Cantat-Gaudin et al. (2019) | 11843 | 11843 | 9246 |
| Damiani et al. (2019) PMS | 10839 | 10839 | 9901 |
| Oh et al. (2017) | 10379 | 0 | 10370 |
| Meingast et al. (2021) | 7925 | 7925 | 5878 |
| Wenger et al. (2000) pMS* | 5901 | 0 | 3006 |
| Gaia Collaboration et al. (2018a) $d < 250 \text{ pc}$ | 5378 | 817 | 3968 |
| Kounkel et al. (2018) | 5207 | 3740 | 5207 |
| Ratzenböck et al. (2020) | 4269 | 4269 | 2662 |
| Wenger et al. (2000) TT* | 4022 | 0 | 3344 |
| Damiani et al. (2019) UMS | 3598 | 3598 | 3598 |
| Rizzuto et al. (2017) | 3294 | 3294 | 2757 |
| Akeson et al. (2013) | 3107 | 868 | 3098 |
| Tian (2020) | 1989 | 1989 | 1394 |
| Goldman et al. (2018) | 1844 | 1844 | 1783 |
| Cotten & Song (2016) | 1695 | 0 | 1693 |
| Gagné et al. (2018b) | 1429 | 0 | 1389 |
| Röser & Schilbach (2020) Psc-Eri | 1387 | 1387 | 1107 |
| Röser & Schilbach (2020) Pleiades | 1245 | 1245 | 1019 |
| Wenger et al. (2000) TT? | 1198 | 0 | 853 |
| Gagné & Faherty (2018) | 914 | 0 | 913 |
| Pavlidou et al. (2021) | 913 | 913 | 504 |
| Gagné et al. (2018a) | 692 | 0 | 692 |
| Ujjwal et al. (2020) | 563 | 0 | 563 |
| Gagné et al. (2020) | 566 | 566 | 351 |
| Esplin & Luhman (2019) | 377 | 443 | 296 |
| Roccatagliata et al. (2020) | 283 | 283 | 232 |
| Meingast & Alves (2019) | 238 | 238 | 238 |
| Fürnkranz et al. (2019) Coma-Ber | 214 | 214 | 213 |
| Fürnkranz et al. (2019) Neighbor Group | 177 | 177 | 167 |
| Kraus et al. (2014) | 145 | 145 | 145 |

NOTE— Table 4 describes the provenances for the young and age-dateable stars in Table 3. N_{Gaia} : number of Gaia stars we parsed from the literature source. N_{Age} : number of stars in the literature source with ages reported. $N_{G_{\text{RP}} < 16}$: number of Gaia stars we parsed from the literature source with either $G_{\text{RP}} < 16$, or a parallax S/N exceeding 5 and a distance closer than 100 pc. The latter criterion included a few hundred white dwarfs that would have otherwise been neglected. Some studies are listed multiple times if they contain multiple tables. Wenger et al. (2000) refers to the SIMBAD database.

REFERENCES

- 856 Agol, E., Luger, R., & Foreman-Mackey, D. 2020, *AJ*,
 857 159, 123
- 858 Akeson, R. L., Chen, X., Ciardi, D., et al. 2013, *PASP*,
 859 125, 989
- 860 Astropy Collaboration, Price-Whelan, A. M., Sipőcz,
 861 B. M., et al. 2018, *AJ*, 156, 123
- 862 Baraffe, I., Homeier, D., Allard, F., & Chabrier, G.
 863 2015, *A&A*, 577, A42
- 864 Beaumont, C., Robitaille, T., Borkin, M., & Goodman,
 865 A. 2014, glueviz v0.4: multidimensional data
 866 exploration
- 867 Benatti, S., Nardiello, D., Malavolta, L., et al. 2019,
 868 *A&A*, 630, A81
- 869 Berger, T. A., Howard, A. W., & Boesgaard, A. M.
 870 2018, *ApJ*, 855, 115
- 871 Berger, T. A., Huber, D., Gaidos, E., & van Saders, J. L.
 872 2018, *ApJ*, 866, 99
- 873 Bhatti, W., Bouma, L. G., & Wallace, J. 2018,
 874 astrobase,
 875 <https://doi.org/10.5281/zenodo.1469822>
- 876 Boisse, I., Pepe, F., Perrier, C., et al. 2012, *A&A*, 545,
 877 A55
- 878 Borucki, W. J., Koch, D., Basri, G., et al. 2010, *Science*,
 879 327, 977
- 880 Bossini, D., Vallenari, A., Bragaglia, A., et al. 2019,
 881 *A&A*, 623, A108
- 882 Bouma, L. G., Curtis, J. L., Hartman, J. D., Winn, J. N.,
 883 & Bakos, G. A. 2021, arXiv:2107.08050 [astro-ph]
- 884 Bouma, L. G., Hartman, J. D., Bhatti, W., Winn, J. N.,
 885 & Bakos, G. Á. 2019, *ApJS*, 245, 13
- 886 Bouma, L. G., Hartman, J. D., Brahm, R., et al. 2020,
 887 *AJ*, 160, 239
- 888 Bressan, A., Marigo, P., Girardi, L., et al. 2012,
 889 *MNRAS*, 427, 127
- 890 Burke, C., & Catanzarite, J. 2021, KeplerPORTS:
 891 Kepler Planet Occurrence Rate Tools
- 892 Burke, C. J., Levine, A., Fausnaugh, M., et al. 2020,
 893 TESS-Point: High precision TESS pointing tool,
 894 Astrophysics Source Code Library, ascl:2003.001
- 895 Cantat-Gaudin, T., & Anders, F. 2020, *A&A*, 633, A99
- 896 Cantat-Gaudin, T., Jordi, C., Vallenari, A., et al. 2018,
 897 *A&A*, 618, A93
- 898 Cantat-Gaudin, T., Jordi, C., Wright, N. J., et al. 2019,
 899 *A&A*, 626, A17
- 900 Cantat-Gaudin, T., Anders, F., Castro-Ginard, A., et al.
 901 2020, *A&A*, 640, A1
- 902 Capitanio, L., Lallement, R., Vergely, J. L., Elyajouri,
 903 M., & Monreal-Ibero, A. 2017, *A&A*, 606, A65
- 904 Castro-Ginard, A., Jordi, C., Luri, X., et al. 2020, *A&A*,
 905 635, A45
- 906 Choi, J., Dotter, A., Conroy, C., et al. 2016, *ApJ*, 823,
 907 102
- 908 Claret, A., & Bloemen, S. 2011, *A&A*, 529, A75
- 909 Cotten, T. H., & Song, I. 2016, *ApJS*, 225, 15
- 910 Dahm, S. E. 2015, *ApJ*, 813, 108
- 911 Dai, F., Winn, J. N., Berta-Thompson, Z.,
 912 Sanchis-Ojeda, R., & Albrecht, S. 2018, *AJ*, 155, 177
- 913 Damiani, F., Prisinzano, L., Pillitteri, I., Micela, G., &
 914 Sciortino, S. 2019, *A&A*, 623, A112
- 915 Davenport, J. R. A. 2016, *ApJ*, 829, 23
- 916 Davenport, J. R. A., Hawley, S. L., Hebb, L., et al.
 917 2014, *ApJ*, 797, 122
- 918 David, T., Hillenbrand, L., & Petigura, E. 2016, *Nature*,
 919 534, 658
- 920 David, T. J., & Hillenbrand, L. A. 2015, *ApJ*, 804, 146
- 921 David, T. J., Petigura, E. A., Luger, R., et al. 2019,
 922 *ApJL*, 885, L12
- 923 David, T. J., Contardo, G., Sandoval, A., et al. 2021, *AJ*,
 924 161, 265
- 925 Dias, W. S., Monteiro, H., Caetano, T. C., et al. 2014,
 926 *A&A*, 564, A79
- 927 Dobbie, P. D., Lodieu, N., & Sharp, R. G. 2010,
 928 *MNRAS*, 409, 1002
- 929 Douglas, S. T., Agüeros, M. A., Covey, K. R., & Kraus,
 930 A. 2017, *ApJ*, 842, 83
- 931 Douglas, S. T., Pérez Chávez, J., Cargile, P. A., et al.
 932 2021, Constraining Stellar Rotation at the ZAMS
- 933 Eggen, O. J. 1968, *ApJ*, 152, 77
- 934 Ehrenreich, D., Bourrier, V., Wheatley, P. J., et al. 2015,
 935 *Nature*, 522, 459
- 936 Esplin, T. L., & Luhman, K. L. 2019, *AJ*, 158, 54
- 937 Feinstein, A. D., Montet, B. T., Johnson, M. C., et al.
 938 2021, arXiv:2107.01213 [astro-ph]
- 939 Foreman-Mackey, D. 2016, *Journal of Open Source
 940 Software*, 1, 24
- 941 Foreman-Mackey, D., Czekala, I., Luger, R., et al. 2020,
 942 exoplanet-dev/exoplanet v0.2.6
- 943 Fulton, B. J., Petigura, E. A., Howard, A. W., et al.
 944 2017, *AJ*, 154, 109
- 945 Fürnkranz, V., Meingast, S., & Alves, J. 2019, *A&A*,
 946 624, L11
- 947 Gagné, J., David, T. J., Mamajek, E. E., et al. 2020,
 948 *ApJ*, 903, 96
- 949 Gagné, J., & Faherty, J. K. 2018, *ApJ*, 862, 138
- 950 Gagné, J., Roy-Loubier, O., Faherty, J. K., Doyon, R.,
 951 & Malo, L. 2018a, *ApJ*, 860, 43

- 952 Gagné, J., Mamajek, E. E., Malo, L., et al. 2018b, *ApJ*,
953 **856**, 23
- 954 Gagné, J., David, T. J., Mamajek, E. E., et al. 2020,
955 *ApJ*, **903**, 96
- 956 Gaia Collaboration, Babusiaux, C., van Leeuwen, F.,
957 et al. 2018a, *A&A*, **616**, A10
- 958 Gaia Collaboration, Brown, A. G. A., Vallenari, A.,
959 et al. 2018b, *A&A*, **616**, A1
- 960 —. 2021a, *A&A*, **649**, A1
- 961 Gaia Collaboration, Smart, R. L., Sarro, L. M., et al.
962 2021b, *A&A*, **649**, A6
- 963 Gelman, A., & Rubin, D. B. 1992, *Statistical Science*, **7**,
964 457, publisher: Institute of Mathematical Statistics
- 965 Gibson, S. R., Howard, A. W., Marcy, G. W., et al. 2016,
966 in *SPIE Conference Series*, Vol. 9908, *Ground-based*
967 and *Airborne Instrumentation for Astronomy VI*, ed.
968 C. J. Evans, L. Simard, & H. Takami, 990870
- 969 Gillen, E., Briegal, J. T., Hodgkin, S. T., et al. 2020,
970 *MNRAS*, **492**, 1008
- 971 Ginsburg, A., Sipocz, B., Madhura Parikh, et al. 2018,
972 *Astropy/Astroquery: V0.3.7 Release*
- 973 Ginzburg, S., Schlichting, H. E., & Sari, R. 2018,
974 *MNRAS*, **476**, 759
- 975 Goldman, B., Röser, S., Schilbach, E., Moór, A. C., &
976 Henning, T. 2018, *ApJ*, **868**, 32
- 977 Guerrero, N. M., Seager, S., Huang, C. X., et al. 2021,
978 *ApJS*, **254**, 39
- 979 Günther, M. N., Zhan, Z., Seager, S., et al. 2020, *AJ*,
980 **159**, 60
- 981 Hattori, S., Foreman-Mackey, D., Hogg, D. W., et al.
982 2021, arXiv e-prints, arXiv:2106.15063
- 983 Hippke, M., David, T. J., Mulders, G. D., & Heller, R.
984 2019, *AJ*, **158**, 143
- 985 Hirano, T., Suto, Y., Taruya, A., et al. 2010, *ApJ*, **709**,
986 458
- 987 Hirano, T., Suto, Y., Winn, J. N., et al. 2011, *ApJ*, **742**,
988 69
- 989 Hoffman, M. D., & Gelman, A. 2014, *Journal of
990 Machine Learning Research*, **15**, 1593
- 991 Holczer, T., Shporer, A., Mazeh, T., et al. 2015, *ApJ*,
992 **807**, 170
- 993 Holczer, T., Mazeh, T., Nachmani, G., et al. 2016,
994 *ApJS*, **225**, 9
- 995 Howard, A. W., Johnson, J. A., Marcy, G. W., et al.
996 2010, *ApJ*, **721**, 1467
- 997 Howell, S. B., Everett, M. E., Sherry, W., Horch, E., &
998 Ciardi, D. R. 2011, *AJ*, **142**, 19
- 999 Ikoma, M., & Hori, Y. 2012, *ApJ*, **753**, 66
- 1000 Ilin, E., Schmidt, S. J., Poppenhöger, K., et al. 2021,
1001 *A&A*, **645**, A42
- 1002 Jones, E., Oliphant, T., Peterson, P., et al. 2001, Open
1003 source scientific tools for Python
- 1004 Kerr, R. M. P., Rizzato, A. C., Kraus, A. L., & Offner,
1005 S. S. R. 2021, *ApJ*, **917**, 23
- 1006 Kharchenko, N. V., Piskunov, A. E., Schilbach, E.,
1007 Röser, S., & Scholz, R.-D. 2013, *A&A*, **558**, A53
- 1008 Kipping, D. M. 2010, *MNRAS*, **408**, 1758
- 1009 Kipping, D. M. 2013, *MNRAS*, **435**, 2152
- 1010 Kite, E. S., Fegley, Jr., B., Schaefer, L., & Ford, E. B.
1011 2020, *ApJ*, **891**, 111
- 1012 Klein, B., & Donati, J.-F. 2020, *MNRAS*, **493**, L92
- 1013 Kounkel, M., & Covey, K. 2019, *AJ*, **158**, 122
- 1014 Kounkel, M., Covey, K., & Stassun, K. G. 2020, *AJ*,
1015 **160**, 279
- 1016 Kounkel, M., Covey, K., Suárez, G., et al. 2018, *AJ*,
1017 **156**, 84
- 1018 Kounkel, M., Covey, K., Suárez, G., et al. 2018, *AJ*,
1019 **156**, 84
- 1020 Kraus, A. L., Ireland, M. J., Huber, D., Mann, A. W., &
1021 Dupuy, T. J. 2016, *AJ*, **152**, 8
- 1022 Kraus, A. L., Shkolnik, E. L., Allers, K. N., & Liu,
1023 M. C. 2014, *AJ*, **147**, 146
- 1024 Lallement, R., Capitanio, L., Ruiz-Dern, L., et al. 2018,
1025 *A&A*, **616**, A132
- 1026 Lindegren, L., Bastian, U., Biermann, M., et al. 2021,
1027 *A&A*, **649**, A4
- 1028 Lomb, N. R. 1976, *Astrophysics and Space Science*, **39**,
1029 447
- 1030 Lopez, E. D., Fortney, J. J., & Miller, N. 2012, *ApJ*,
1031 **761**, 59
- 1032 Luger, R., Agol, E., Foreman-Mackey, D., et al. 2019,
1033 *AJ*, **157**, 64
- 1034 Mann, A. W., Newton, E. R., Rizzato, A. C., et al. 2016,
1035 *AJ*, **152**, 61
- 1036 Mann, A. W., Johnson, M. C., Vanderburg, A., et al.
1037 2020, *AJ*, **160**, 179
- 1038 Martioli, E., Hébrard, G., Correia, A. C. M., Laskar, J.,
1039 & Lecavelier des Etangs, A. 2021, *A&A*, **649**, A177
- 1040 Masuda, K. 2015, *ApJ*, **805**, 28
- 1041 Mazeh, T., Holczer, T., & Shporer, A. 2015, *ApJ*, **800**,
1042 142
- 1043 McCann, J., Murray-Clay, R. A., Kratter, K., &
1044 Krumholz, M. R. 2019, *ApJ*, **873**, 89
- 1045 McKinney, W. 2010, in *Proceedings of the 9th Python
1046 in Science Conference*, ed. S. van der Walt &
1047 J. Millman, 51
- 1048 McQuillan, A., Mazeh, T., & Aigrain, S. 2014, *ApJS*,
1049 **211**, 24
- 1050 Meibom, S., Mathieu, R. D., & Stassun, K. G. 2007,
1051 *ApJL*, **665**, L155

- 1052 Meibom, S., Barnes, S. A., Latham, D. W., et al. 2011,
 1053 *ApJL*, **733**, L9
- 1054 Meibom, S., Torres, G., Fressin, F., et al. 2013, *Nature*,
 1055 **499**, 55
- 1056 Meingast, S., & Alves, J. 2019, *A&A*, **621**, L3
- 1057 Meingast, S., Alves, J., & Rottensteiner, A. 2021, *A&A*,
 1058 **645**, A84
- 1059 Montet, B. T., Tovar, G., & Foreman-Mackey, D. 2017,
 1060 *ApJ*, **851**, 116
- 1061 Montet, B. T., Feinstein, A. D., Luger, R., et al. 2020,
 1062 *AJ*, **159**, 112
- 1063 Morris, B. M. 2020, *ApJ*, **893**, 67
- 1064 Morton, T. D., Bryson, S. T., Coughlin, J. L., et al.
 1065 2016, *ApJ*, **822**, 86
- 1066 Narita, N., Fukui, A., Yamamoto, T., et al. 2020, in
 1067 *SPIE Conference Series*, 114475K
- 1068 Newton, E. R., Mann, A. W., Tofflemire, B. M., et al.
 1069 2019, *ApJ*, **880**, L17
- 1070 Oh, S., Price-Whelan, A. M., Hogg, D. W., Morton,
 1071 T. D., & Spergel, D. N. 2017, *AJ*, **153**, 257
- 1072 Owen, J. E. 2020, *MNRAS*, **498**, 5030
- 1073 Owen, J. E., & Wu, Y. 2013, *ApJ*, **775**, 105
 1074 —. 2016, *ApJ*, **817**, 107
- 1075 Palle, E., Oshagh, M., Casasayas-Barris, N., et al. 2020,
 1076 *A&A*, **643**, 25
- 1077 Pavlidou, T., Scholz, A., & Teixeira, P. S. 2021,
 1078 *MNRAS*, **503**, 3232
- 1079 Pecaut, M. J., & Mamajek, E. E. 2013, *ApJS*, **208**, 9
- 1080 Pecaut, M. J., & Mamajek, E. E. 2016, *MNRAS*, **461**,
 1081 794
- 1082 Plavchan, P., Barclay, T., Gagné, J., et al. 2020, *Nature*,
 1083 **582**, 497
- 1084 Poppenhaeger, K., Ketzer, L., & Mallonn, M. 2021,
 1085 *MNRAS*, **500**, 4560
- 1086 Randich, S., Tognelli, E., Jackson, R., et al. 2018, *A&A*,
 1087 **612**, A99
- 1088 Ratzenböck, S., Meingast, S., Alves, J., Möller, T., &
 1089 Bomze, I. 2020, *A&A*, **639**, A64
- 1090 Rebull, L. M., Stauffer, J. R., Bouvier, J., et al. 2016,
 1091 *AJ*, **152**, 113
- 1092 Reinhold, T., & Hekker, S. 2020, *A&A*, **635**, A43
- 1093 Ricker, G. R., Winn, J. N., Vanderspek, R., et al. 2015,
 1094 *JATIS*, **1**, 014003
- 1095 Rizzuto, A. C., Mann, A. W., Vanderburg, A., Kraus,
 1096 A. L., & Covey, K. R. 2017, *AJ*, **154**, 224
- 1097 Rizzuto, A. C., Newton, E. R., Mann, A. W., et al. 2020,
 1098 *AJ*, **160**, 33
- 1099 Roccatagliata, V., Franciosini, E., Sacco, G. G.,
 1100 Randich, S., & Sicilia-Aguilar, A. 2020, *A&A*, **638**,
 1101 A85
- 1102 Roettenbacher, R. M., Monnier, J. D., Korhonen, H.,
 1103 et al. 2017, *ApJ*, **849**, 120
- 1104 Röser, S., & Schilbach, E. 2020, *A&A*, **638**, A9
- 1105 Salvatier, J., Wiecki, T. V., & Fonnesbeck, C. 2016,
 1106 PyMC3: Python probabilistic programming
 1107 framework
- 1108 Scargle, J. D. 1982, *ApJ*, **263**, 835
- 1109 Scott, N. J., Howell, S. B., Horch, E. P., & Everett,
 1110 M. E. 2018, *PASP*, **130**, 054502
- 1111 Scott, N. J., Howell, S. B., Gnilka, C. L., et al. 2021,
 1112 *Frontiers in Astronomy and Space Sciences*, **8**, 138
- 1113 Seifahrt, A., Stürmer, J., Bean, J. L., & Schwab, C.
 1114 2018, in *SPIE Conference Series*, Vol. 10702,
 1115 *Ground-based and Airborne Instrumentation for
 1116 Astronomy VII*, ed. C. J. Evans, L. Simard, &
 1117 H. Takami, 107026D
- 1118 Shapiro, A. I., Solanki, S. K., Krivova, N. A., Yeo,
 1119 K. L., & Schmutz, W. K. 2016, *A&A*, **589**, A46
- 1120 Shporer, A., Zhou, G., Vanderburg, A., et al. 2017,
 1121 *ApJL*, **847**, L18
- 1122 Skrutskie, M. F., Cutri, R. M., Stiening, R., et al. 2006,
 1123 *AJ*, **131**, 1163
- 1124 Smith, J. C., Morris, R. L., Jenkins, J. M., et al. 2016,
 1125 *PASP*, **128**, 124501
- 1126 Smith, J. C., Stumpe, M. C., Jenkins, J. M., et al. 2017,
 1127 *Kepler Science Document*, 8
- 1128 Soderblom, D. R., Hillenbrand, L. A., Jeffries, R. D.,
 1129 Mamajek, E. E., & Naylor, T. 2014, *Protostars and
 1130 Planets VI*, 219
- 1131 Spake, J. J., Sing, D. K., Evans, T. M., et al. 2018,
 1132 *Nature*, **557**, 68
- 1133 Stassun, K. G., Oelkers, R. J., Paegert, M., et al. 2019,
 1134 *AJ*, **158**, 138
- 1135 Stauffer, J., Rebull, L., Bouvier, J., et al. 2016, *AJ*, **152**,
 1136 115
- 1137 Stauffer, J. R., Hartmann, L. W., Prosser, C. F., et al.
 1138 1997, *ApJ*, **479**, 776
- 1139 Stefansson, G., Mahadevan, S., Maney, M., et al. 2020,
 1140 *AJ*, **160**, 192
- 1141 Stephenson, C. B. 1959, *PASP*, **71**, 145
- 1142 Strassmeier, K. G. 2009, *Astronomy and Astrophysics
 1143 Review*, **17**, 251
- 1144 Tenenbaum, P., Christiansen, J. L., Jenkins, J. M., et al.
 1145 2012, *ApJS*, **199**, 24
- 1146 Theano Development Team. 2016, *arXiv e-prints*,
 1147 [abs/1605.02688](https://arxiv.org/abs/1605.02688)
- 1148 Thompson, S. E., Coughlin, J. L., Hoffman, K., et al.
 1149 2018, *ApJS*, **235**, 38
- 1150 Tian, H.-J. 2020, *ApJ*, **904**, 196
- 1151 Tofflemire, B. M., Rizzuto, A. C., Newton, E. R., et al.
 1152 2021, *AJ*, **161**, 171

- 1153 Ujjwal, K., Kartha, S. S., Mathew, B., Manoj, P., &
 1154 Narang, M. 2020, *AJ*, **159**, 166
 1155 Van Eylen, V., Agentoft, C., Lundkvist, M. S., et al.
 1156 2018, *MNRAS*, **479**, 4786
 1157 Van Eylen, V., Albrecht, S., Huang, X., et al. 2019, *AJ*,
 1158 **157**, 61
 1159 Villa Vélez, J. A., Brown, A. G. A., & Kenworthy,
 1160 M. A. 2018, *RNAAS*, **2**, 58
 1161 Vissapragada, S., Knutson, H. A., Jovanovic, N., et al.
 1162 2020, *AJ*, **159**, 278
 1163 Vogt, S. S., Allen, S. L., Bigelow, B. C., et al. 1994,
 1164 SPIE Conference Series, ed. D. L. Crawford & E. R.
 1165 Craine, Vol. 2198
 1166 Walkowicz, L. M., & Basri, G. S. 2013, *MNRAS*, **436**,
 1167 **1883**, arXiv: 1309.2159
 1168 Wang, L., & Dai, F. 2019, *ApJL*, **873**, L1
 1169 Wenger, M., Ochsenbein, F., Egret, D., et al. 2000,
 1170 *A&AS*, **143**, 9
 1171 Wirth, C. P., Zhou, G., Quinn, S. N., et al. 2021, *ApJL*,
 1172 **917**, L34
 1173 Wu, Y. 2019, *ApJ*, **874**, 91
 1174 Yee, S. W., Petigura, E. A., & von Braun, K. 2017, *ApJ*,
 1175 **836**, 77
 1176 Yelda, S., Lu, J. R., Ghez, A. M., et al. 2010, *ApJ*, **725**,
 1177 **331**
 1178 Zari, E., Hashemi, H., Brown, A. G. A., Jardine, K., &
 1179 de Zeeuw, P. T. 2018, *A&A*, **620**, A172
 1180 Zhou, G., Winn, J. N., Newton, E. R., et al. 2020, *ApJ*,
 1181 **892**, L21
 1182 Zhou, G., Quinn, S. N., Irwin, J., et al. 2021, *AJ*, **161**, 2

1183

APPENDIX

1184

A. YOUNG, AGE-DATED, AND AGE-DATEABLE STAR COMPILED

1185 The v0.6 CDIPS target catalog (Table 3) includes stars that are young, age-dated, and age-dateable. By
 1186 “age-dateable”, we mean that the stellar age should be measurable at greater precision than that of a typical
 1187 FGK field star, through either isochronal, gyrochronal, or spectroscopic techniques. As in Bouma et al.
 1188 (2019), we collected stars that met these criteria from across the literature. Table 4 gives a list of the studies
 1189 included, and brief summary statistics. The age measurement methodologies adopted by each study differ: in
 1190 many, spatial and kinematic clustering has been performed on the Gaia data, and ensemble isochrone fitting
 1191 of the resulting clusters has been performed (typically focusing on the turn-off). In other studies however,
 1192 the claim of youth is based on the location of a single star in the color-absolute magnitude diagram, or on
 1193 spectroscopic information.

1194 One major change in Table 3 relative to the earlier iteration from Bouma et al. (2019) is that the extent
 1195 of Gaia-based analyses has now matured to the point that we can neglect pre-Gaia cluster memberships,
 1196 except for a few cases with spectroscopically confirmed samples of age-dated stars. The membership lists for
 1197 instance of Kharchenko et al. (2013) and Dias et al. (2014) (MWSC and DAML) are no longer required. This
 1198 is helpful for various post-processing projects, since the field star contamination rates were typically much
 1199 higher in these catalogs than in the newer Gaia-based catalogs.

1200 The most crucial parameters of a given star for our purposes are the Gaia DR2 `source_id`, the cluster
 1201 or group name (`cluster`), and the `age`. Given the hierarchical nature of many stellar associations, we do
 1202 not attempt to resolve the cluster names to a single unique string. The Orion complex for instance can be
 1203 divided into almost one hundred kinematic subgroups (Kounkel et al. 2018). (**Added: Based on Figure 1,**
 1204 **the δ Lyr cluster may also be part of a similar hierarchical association.**) Similar complexity applies to the
 1205 problem of determining homogeneous ages, which we do not attempt to resolve. Instead, we simply merged
 1206 the cluster names and ages reported by various authors into a comma-separated string.

1207 This means that the `age` column can be null, for cases in which the original authors did not report an age,
 1208 or for which a reference literature age was not readily available. Nonetheless, since we do prefer stars with
 1209 known ages, we made a few additional efforts to populate this column. When available, the age provenance
 1210 is from the original analysis of the cluster. In a few cases however we adopted other ages when string-
 1211 based cross-matching on the cluster name was straightforward. In particular, we used the ages determined
 1212 by Cantat-Gaudin et al. (2020) to assign ages to the clusters from Gaia Collaboration et al. (2018a), Cantat-
 1213 Gaudin et al. (2018), Castro-Ginard et al. (2020), and Cantat-Gaudin & Anders (2020).

1214 The catalogs we included for which ages were not immediately available were those of Cotten & Song
 1215 (2016), Oh et al. (2017), Zari et al. (2018), Gagné et al. (2018a), Gagné et al. (2018b), Gagné & Faherty
 1216 (2018), and Ujjwal et al. (2020). While in principle the moving group members discussed by Gagné et al.
 1217 (2018a,b); Gagné & Faherty (2018) and Ujjwal et al. (2020) have easily associated ages, our SIMBAD cross-
 1218 match did not retain the moving group identifiers given by those studies, which should therefore be recovered
 1219 using tools such as BANYAN Σ (Gagné et al. 2018b). We also included the SIMBAD object identifiers `TT*`,
 1220 `Y*O,Y*?`, `TT?`, and `pMS*`. Finally, we included every star in the NASA Exoplanet Archive planetary system
 1221 (`ps`) table that had a Gaia identifier available (Akeson et al. 2013). If the age had finite uncertainties, we also
 1222 included it, since stellar ages determined through the combination of isochrone-fitting and transit-derived
 1223 stellar densities typically have higher precision than from isochrones alone.

1224 For any of the catalogs for which Gaia DR2 identifiers were not available, we either followed the spatial
 1225 (plus proper-motion) cross-matching procedures described in Bouma et al. (2019), or else we pulled the
 1226 Gaia DR2 source identifiers associated with the catalog from SIMBAD. We consequently opted to drop the
 1227 `ext_catalog_name` and `dist` columns maintained in Bouma et al. (2019), as these were only popu-
 1228 lated for a small number of stars. The technical manipulations for the merging, cleaning, and joining were
 1229 performed using pandas (McKinney 2010). The eventual cross-match (using the Gaia DR2 `source_id`)
 1230 against the Gaia DR2 archive was performed asynchronously on the Gaia archive website.

1231

B. THE TRANSIT ASYMMETRY

1232

B.1. How Robust is the Asymmetric Transit?

1233 As a means of exploring the robustness of the transit asymmetry, Figures 9, 10, and 11 show the Kepler data
 1234 binned in three ways: over Kepler quarters, Julian years, and quartiles of local slope. Over Kepler quarters
 1235 (Figure 9), Quarter 6 shows the strongest asymmetry: a deviation of about 3 ppt from expectation. Quarter

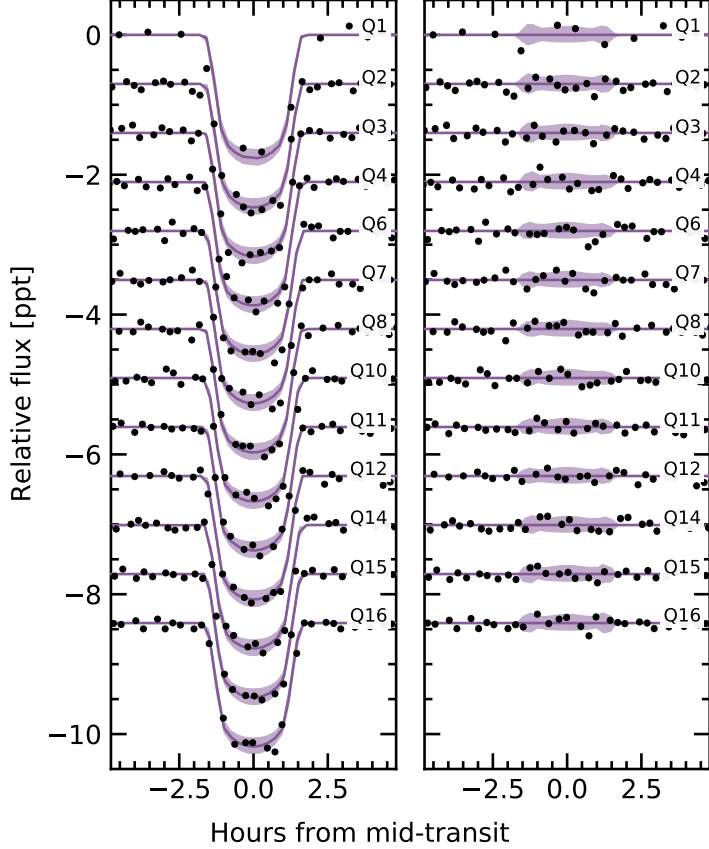


Figure 9. Transit model residuals through time (binned by Kepler quarter). *Left:* Phase-folded transit of Kepler 1627b, with stellar variability removed. Black points are binned to 20 minute intervals. The 2σ model uncertainties and the maximum *a posteriori* model are shown as the faint purple band, and the dark purple line. *Right:* As on the left, with the transit removed.

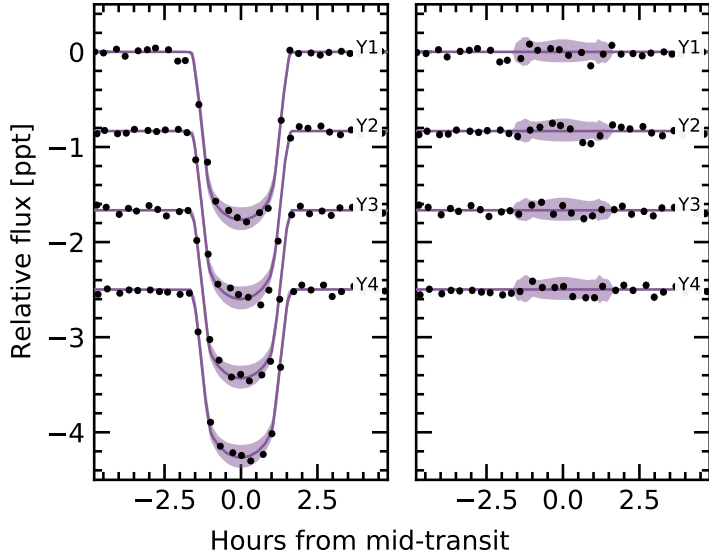


Figure 10. Transit model residuals through time (binned by year of observation). *Left:* Phase-folded transit of Kepler 1627b, with stellar variability removed. Points and models are as in Figure 9. *Right:* As on the left, with the transit removed.

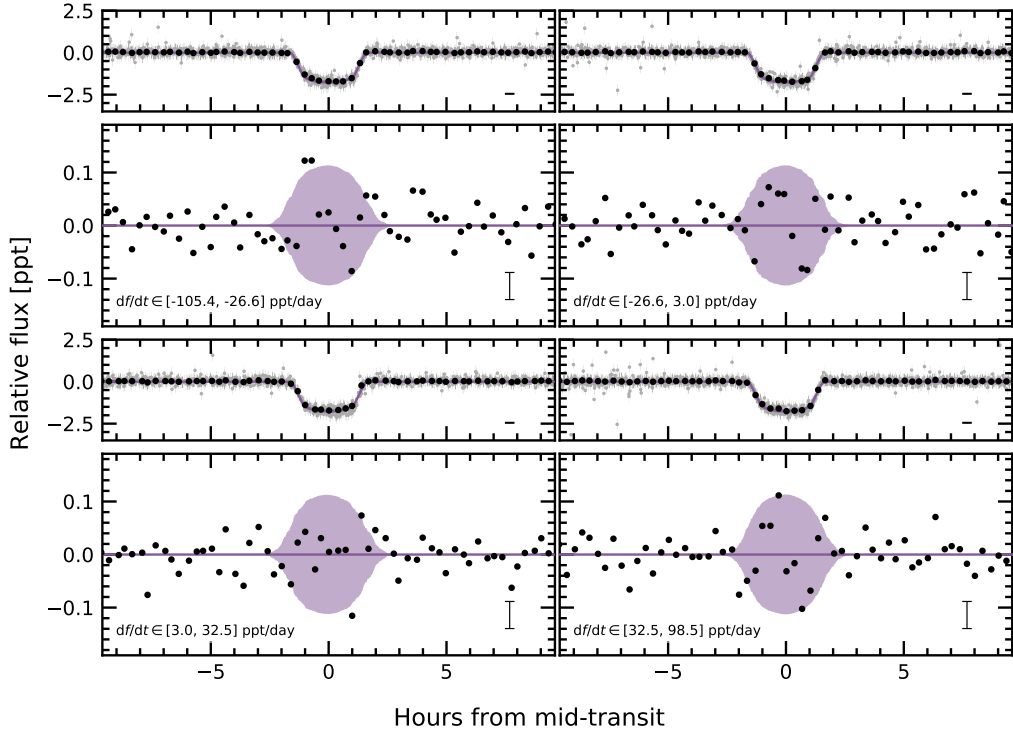


Figure 11. Transit models and residuals, binned by quartiles in the local slope of the light curve. Representative uncertainties for the black points (binned at 20 minute intervals) are shown in the lower right of each panel. A similar transit asymmetry to that shown in Figure 5 seems to be present in three of the four bins.

1236 7 shows an anomaly at roughly the same transit phase. Year 2 correspondingly shows the strongest anomaly
 1237 out of any year in Figure 10; the asymmetry is visually apparent however in each of the four years.

1238 To bin by quartiles in local slope, we used our measurements of the local linear slopes in each of the
 1239 observed transit windows (144 transits total). Four outlier transits were removed, leaving 140 transits. These
 1240 were then divided into quartiles, so that each panel shows 35 transits binned together. The exact light curve
 1241 slope intervals are listed in the lower left panels of Figure 11. Binned by local slope quartiles (Figure 11),
 1242 the asymmetry is visually present in three of the four quartiles: the only bin in which it does not appear is
 1243 $df/dt \in [3.0, 32.5] \text{ ppt day}^{-1}$.

1244 Within the theory presented by Mazeh et al. (2015), unresolved starspot crossings cause the weak correlation
 1245 between TTVs and the local light curve slope (Figure 6). In this model, we would expect the light curves
 1246 with the most negative local slopes to have the largest positive TTVs, due to spot crossing events during the
 1247 latter half of transit. The upper-left panel of Figure 11 agrees with this expectation. However, we would also
 1248 expect the sign of the effect to reverse when considering the most positive local slopes (most negative TTVs).
 1249 The lower-right panel of Figure 11 contradicts this expectation: the residual in both cases maintains the same
 1250 parity! On the one hand, this shows that the residual is not dependent on the local light curve slope, which
 1251 lowers the likelihood that it might be an artifact of our detrending methods. On the other, it raises the question
 1252 of whether unresolved starspot crossings are indeed the root cause of the correlation shown in Figure 6. While
 1253 we do not have a solution to this contradiction, the injection-recovery tests discussed in Section 4.1.3 provide
 1254 some assurance that the TTV-slope correlation is not simply a systematic artifact.

1255 B.2. Interpretation

1256 The transit asymmetry seems robust against most methods of binning the data, though with some caveats
 1257 (e.g., the “middle quartile” in local flux, $df/dt \in [3.0, 32.5] \text{ ppt day}^{-1}$, where the asymmetry does not appear).
 1258 Nonetheless, if the asymmetric were systematic we might expect its parity to reverse as a function of the sign
 1259 of the local slope, and it does not. We therefore entertained four possible astrophysical explanations: gravity
 1260 darkening, transit timing variations, spot-crossing events, and a persistent asymmetric dusty outflow.

1261 Gravity darkening is based on the premise that the rapidly rotating star is oblate, and brighter near the
 1262 poles than the equator (e.g., Masuda 2015). The fractional transit shape change due to gravity darkening
 1263 is on the order of $(P_{\text{break}}/P_{\text{rot}})^2$, for P_{break} the break-up rotation period, and P_{rot} the rotation period. Using

1264 the parameters from Table 2, this yields an expected 0.14% distortion of the \approx 1.8 ppt transit depth: *i.e.*, an
 1265 absolute deviation of \approx 2.5 ppm. The observed residual has a semi-amplitude of \approx 50 ppm. Since the expected
 1266 signal is smaller than the observed anomaly by over an order of magnitude, gravity darkening seems to be an
 1267 unlikely explanation.

1268 The scenario of transit timing variations (TTVs) producing the asymmetry seems unlikely because the transit
 1269 timing variations we do observe are correlated with the local light curve slope, which increases roughly as
 1270 much as it decreases. From our analysis, the mean TTV and its standard deviation are 0.66 ± 5.53 min;
 1271 similarly the mean local slope and its standard deviation are 0.59 ± 45.50 ppt day $^{-1}$. There is therefore little
 1272 expectation for TTVs to produce the asymmetry. A separate line of argument comes from Figure 11. If the
 1273 local slope were essential to producing the transit asymmetry, we would expect that in the largest df/dt bin,
 1274 $df/dt \in [3.0, 32.5]$ ppt day $^{-1}$, the sign of the asymmetry would reverse. We do not see evidence for this being
 1275 the case.

1276 The third and related possibility is that of starspot crossings. Young stars have higher spot-covering frac-
 1277 tions than old stars (*e.g.*, Morris 2020). Young solar-type stars may also host dark starspots at high stellar
 1278 latitudes (*e.g.*, EK Dra; Strassmeier 2009), though interferometric imaging of spotted giant stars has shown
 1279 different starspot latitude distributions than those inferred from Doppler imaging (Roettenbacher et al. 2017).
 1280 Regardless, for any spot-crossing anomalies to add coherently over the 140 Kepler transits, it seems likely
 1281 that we would need either for spots to be persistent at a particular latitude (and for the planetary orbit to be
 1282 somewhat misaligned), or for a “stroboscopic” longitudinal phasing (*e.g.*, Dai et al. 2018). For our system,
 1283 $P_{\text{orb}}/P_{\text{rot}} \approx 2.76$, which means that every 4 transits and 11 stellar rotations, the planet crosses over roughly the
 1284 same stellar longitude, which might enable the necessary phasing if the spot-groups are large and long-lived.
 1285 Unfortunately, the S/N per Kepler transit is ≈ 8 , which renders individual spot-crossing events unresolved.
 1286 This explanation seems marginally plausible, mainly because the expected spot-crossing anomaly amplitudes
 1287 (≈ 100 ppm) resemble the observed amplitude of the asymmetry (≈ 50 ppm). One issue with this explanation
 1288 however is that there is no reason to expect starspot crossing events to last exactly half the transit duration.

1289 A persistent feature of the planet itself might therefore be needed to explain the transit asymmetry. An
 1290 asymmetric outflow from the planet’s atmosphere could at least geometrically meet the requirements (*e.g.*,
 1291 McCann et al. 2019). To explain the asymmetric transit, a small, dense component would lead the planet,
 1292 and a long, more rarefied (and variable) component would trail it. This might also explain the slight flux
 1293 decrement visible for \sim 1 hour pre-ingress (Figure 5). The amplitude of the asymmetry is roughly in line
 1294 with theoretical expectations for dusty outflows (Wang & Dai 2019), and based on the planet’s size, its mass
 1295 is likely in a regime where such outflows are possible. Out of the four explanations discussed, this one at
 1296 least theoretically seems the most plausible. By composition, the expectation would be that the envelope
 1297 is mostly hydrogen and helium gas, with a dust or haze component providing the broadband opacity in the
 1298 Kepler bandpass. A natural path for testing this idea would be to observe additional transits of the planet in
 1299 hydrogen absorption, metastable helium absorption, or across a broad wavelength range in the near-infrared.

1300 C. SPECTROSCOPY AND PHOTOMETRY DURING THE TRANSIT OF 2021 AUG 7

1301 We monitored Kepler 1627 with Keck/HIRES before, during, and after transit on the night of 2021 Aug
 1302 7. We used the iodine cell for wavelength calibration, and extracted the 1-D spectra using the standard
 1303 California Planet Survey pipeline (Howard et al. 2010). The airmass ranged between 1.1 and 2.2 from the
 1304 start through the end of observations; the seeing ranged from 1. $''$ 1 at the beginning to 1. $''$ 5 at the end. We
 1305 also simultaneously observed across *griz* bands using MuSCAT3 at Haleakalā Observatory on Maui, HI.
 1306 Performing aperture photometry on the latter image stack yielded the data given in Table 5.

1307 We considered two approaches to measuring the velocities: in the first, hereafter “Method 1”, we cross-
 1308 correlated against a template found via spectral classification with SpecMatch-Emp (Yee et al. 2017). In
 1309 “Method 2”, we used a high S/N template of V1298 Tau. Although V1298 Tau is cooler than Kepler 1627A
 1310 by \approx 500 K, it has a comparable amount of line-broadening ($v \sin i = 23$ km s $^{-1}$), and a comparable level of
 1311 stellar activity. The mean and standard deviation of the internal RV uncertainties averaged over all epochs
 1312 were 16.2 ± 1.1 m s $^{-1}$ from Method 1, and 12.6 ± 0.6 m s $^{-1}$ from Method 2. The corresponding time-averaged
 1313 reduced χ^2 from the template match was 1.57 ± 0.04 (Method 1) and 1.30 ± 0.02 (Method 2). Given these
 1314 diagnostics, we adopted the velocities from the second approach, which are reported in Table 6.

1315 Figure 7 shows the results. The MuSCAT3 photometry shows the expected starspot trend, along with the
 1316 transit and what is likely a chromatic starspot crossing event at JD $- 2459433 = 0.955$. The radial velocities
 1317 decrease by \approx 250 m s $^{-1}$ over the six hour window. This decrease in RV is correlated with a decrease in
 1318 the S-indices derived from the Ca HK lines. One outlying RV point is apparent shortly before egress; it is
 1319 temporally coincident with an outlying value in the S-index time series.

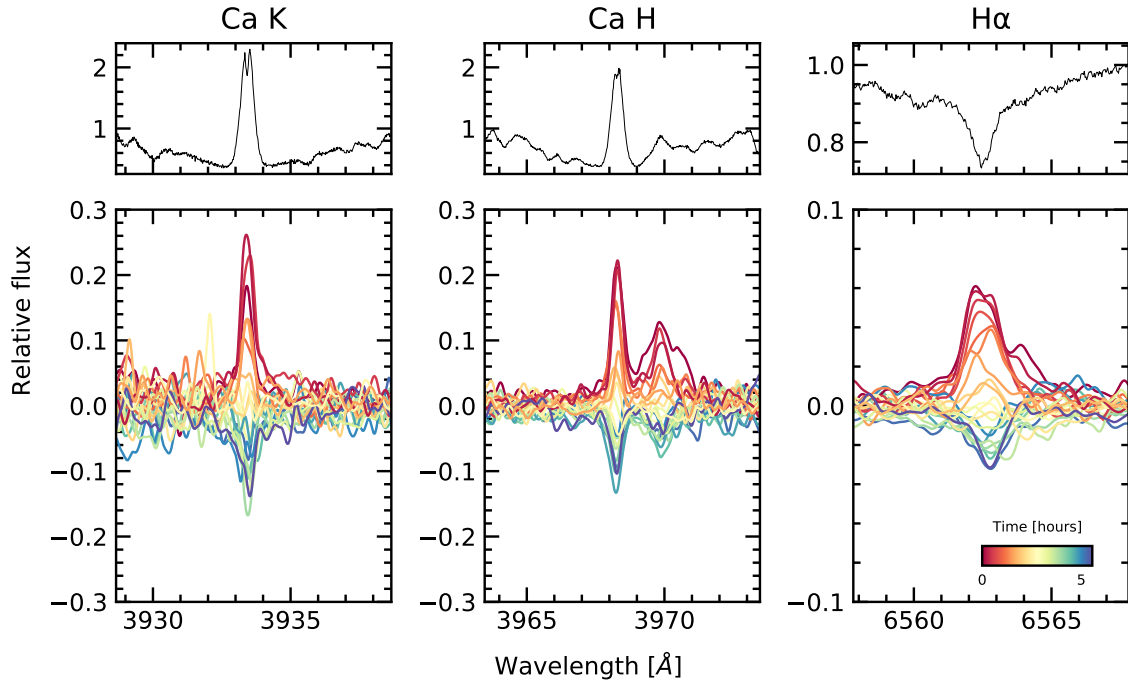


Figure 12. Spectroscopic activity indicators during the transit of 2021 Aug 7. The *top panels* show the median line profiles Ca K, Ca H, and H α line profiles from the HIRES spectra. The *lower panels* show the differences of each individual spectrum relative to the median spectrum. The bump in the red wing of Ca H is He. The spectra in the lower panels are smoothed for visualization purposes.

Overall, we expect the dominant trends in both the photometry and radial velocities to be caused by starspots on the stellar photosphere rotating into and out of view. The plasma in the leading and receding limbs of the stellar disk has an apparent line-of-sight velocity of $\pm 20 \text{ km s}^{-1}$. Over 10% of a rotation cycle ($P_{\text{rot}} = 2.6 \text{ days}$), spots near these limbs come into and out of view, modulate the stellar velocity profile, and can thereby produce the overall $\approx 250 \text{ m s}^{-1}$ trend. The Ca HK and H α emission profiles support this interpretation; Figure 12 shows that each line gradually decreases in intensity over the course of the six hour sequence.

The expectation however is for the starspot-induced signals to be smooth, at worst with contributions at $0.5 P_{\text{rot}}$ or $0.25 P_{\text{rot}}$ (Klein & Donati 2020). We therefore fitted the RVs using the Hirano et al. (2010, 2011) models for the Rossiter-McLaughlin (RM) effect, and allowed for an optional linear and quadratic trend in time to fit the $\approx 250 \text{ m s}^{-1}$ spot-induced trend. We followed the methodology developed by Stefansson et al. (2020). We allowed the sky-projected obliquity, the projected stellar equatorial velocity, and the Gaussian dispersion of the spectral lines to vary, and fixed the limb-darkening using the V-band tabulation from Claret & Bloemen (2011). We assumed a Gaussian prior on $v \sin i$ and a/R_{\star} from Table 1, and also allowed for a white-noise jitter term to be added in quadrature to the measurement uncertainties. We used a 15 minute exposure time to numerically evaluate the model.

The quadratic model with the RM effect is shown in Figure 7; the jitter term is incorporated in the model uncertainties, but not the plotted measurement uncertainties. The plotted measurement uncertainties are the internal uncertainties on the RVs ($\approx 13 \text{ m s}^{-1}$), and are dominated by the $v \sin i$ broadening. However, between exposures, the RVs show significant additional scatter that is not captured by the slow quadratic trend. The white-noise jitter for this particular model is $\sigma_{\text{RV}} = 27^{+6}_{-5} \text{ m s}^{-1}$, which is comparable to the expected RM anomaly of $\Delta v_{\text{RM}} \approx f_{\text{LD}} \cdot \delta \cdot v \sin i \cdot \sqrt{1 - b^2} \approx 20 \text{ m s}^{-1}$, assuming a perfectly aligned orbit.

The presence of this additional scatter prevents a convincing detection of the RM effect. The reason can be understood via model comparison. If we compare the model with a quadratic trend and the RM effect against a model with a linear trend and the RM effect, or even a model with no RM effect at all, then the respective

Bayesian Information Criterion (BIC) values are as follows.

$$\begin{aligned} \text{BIC} &= 227.1 \quad (\text{Quadratic+RM}) \\ \text{BIC} &= 231.1 \quad (\text{Linear+RM}) \\ \text{BIC} &= 221.4 \quad (\text{Only Quadratic}). \end{aligned} \quad (\text{C1})$$

1341 There is therefore no evidence to prefer the model with the RM effect against a model that only accounts
 1342 for the stellar variability. The “only quadratic” model does particularly well because it can inflate the jitter
 1343 term to account for scatter during the transit (even if the scatter contains astrophysics!), and it has fewer free
 1344 parameters. However, we cannot justify a physical prior on the jitter term, because we do not understand
 1345 the origin of the exposure-to-exposure scatter. As noted above, the velocity deviations from starspots are
 1346 expected to have contributions at the stellar rotation frequency, or harmonics thereof. This jitter is present on
 1347 the exposure timescale (15 minutes), which is only 0.4% of the stellar rotation period; it is not obvious that
 1348 starspots would be the culprit.

1349 The amplitude of both the spot-induced trend and the jitter are somewhat larger than recent comparable
 1350 measurements in systems such as AU Mic (Palle et al. 2020), DS Tuc (Montet et al. 2020; Zhou et al. 2020)
 1351 and TOI 942 (Wirth et al. 2021). One possible explanation for the jitter is that it is astrophysical in origin,
 1352 and that it is caused by some novel process operating on the surface of Kepler 1627A. Another possibility
 1353 is that our RV analysis underestimates our measurement uncertainties; in order to achieve the requisite time-
 1354 sampling the S/N per resolution element in our spectra was 70 to 80, which is lower than desired for deriving
 1355 high-precision velocities. In addition, the rapid rotation of the star could affect accuracy of the uncertainties
 1356 from the velocity extraction. Observations at higher S/N are necessary to distinguish these two possibilities,
 1357 and remain worthwhile in order to clarify the orbital geometry of Kepler 1627Ab. Useful next steps would
 1358 include transit observations with a stabilized spectrograph in the optical (e.g., Gibson et al. 2016; Seifahrt
 1359 et al. 2018), or in the near-infrared (e.g., Feinstein et al. 2021).

Table 5. MuSCAT3 photometry of Kepler 1627.

| Time [BJD _{TDB}] | Rel. Flux | Rel. Flux Err. | Bandpass |
|----------------------------|-----------|----------------|----------|
| 2459433.829202 | 0.99719 | 0.00091 | g |
| 2459433.829324 | 0.99849 | 0.00112 | r |
| 2459433.829117 | 0.99611 | 0.00116 | i |
| 2459433.829406 | 0.99941 | 0.00136 | z |

NOTE— Table 5 is published in its entirety in a machine-readable format. Example entries are shown for guidance regarding form and content.

Table 6. Kepler 1627 radial velocities.

| Time [BJD _{TDB}] | RV [m s^{-1}] | σ_{RV} [m s^{-1}] | S-value |
|----------------------------|--------------------------|--|---------|
| 2459433.801306 | 152.97 | 12.29 | 0.7355 |
| 2459433.812255 | 100.5 | 13.23 | 0.7434 |

NOTE— Table 6 is published in its entirety in a machine-readable format. Example entries are shown for guidance regarding form and content.

D. FLARE ANALYSIS

1360
 1361 In addition to the 3.9 years of long cadence data,
 1362 short cadence (1-minute) Kepler observations were
 1363 acquired over 97.7 days during Quarter 15. The
 1364 short cadence light curve shows a higher rate of
 1365 flaring than visible in the long cadence data (Figure
 1366 13). We analyzed the short cadence light curve
 1367 and its flares according to the following procedure.

- 1368 1. Fit the starspot-induced variability using a
 1369 Gaussian Process with a SHOTerm kernel,
 1370 a white-noise jitter term, and the mean flux.

 1371 2. Select points more than twice the median ab-
 1372 solute deviation from the residual, and ex-
 1373 clude them from the light curve (these points
 1374 include the flares). Repeat Step 1.

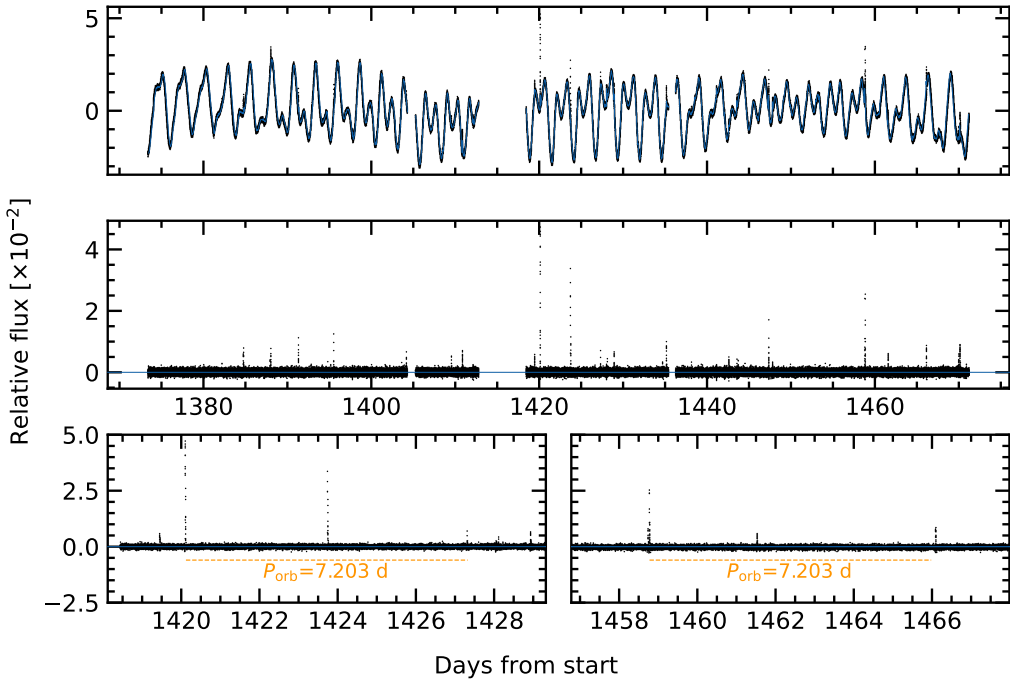


Figure 13. Flares in Kepler 1627. *Top:* The 1-minute cadence Kepler data (black points) is shown with a stellar variability model superposed (blue line). *Middle:* Residual after subtracting the stellar variability model. Flares appear as spikes. *Bottom:* Zooms of the brightest, and third-brightest flares. A timing coincidence – that both flares have “successors” approximately one (Added: planetary) orbital period after the initial event – is emphasized.

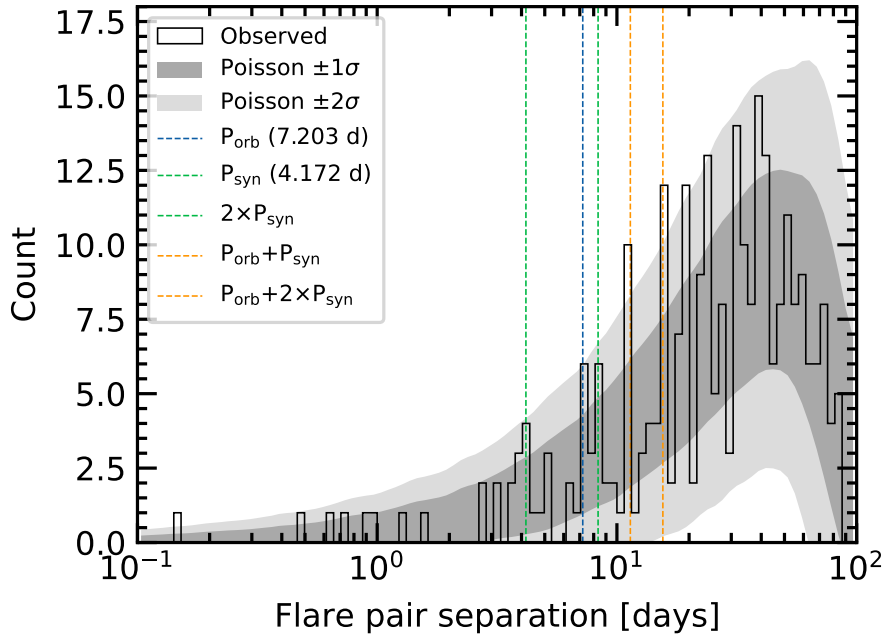


Figure 14. Statistics of inter-flare arrival times. 24 flares were recorded with amplitudes exceeding 0.5% over the 97.7 days of short cadence observations. The histogram of the time intervals between every possible pair of flares is shown in black. Some plausibly important timescales for star-planet interactions, namely the planetary orbital period and synodic period (the orbital period as seen from the rotating stellar frame) are shown along with their linear combinations. Monte Carlo draws from a Poisson distribution are shown with the gray bands. While peaks in the observed distribution do coincide with some of the “special periods”, the statistical evidence for a non-Poissonian process driving the flares does not clear the 5σ threshold.

1375 3. Using the residual from Step 2, identify all
 1376 flares, requiring them to be at least 20 ca-
 1377 dences apart, at least 7 median absolute de-
 1378 viations above the median baseline, and last-
 1379 ing at least 2 cadences in duration. Build the
 1380 mask spanning these times, from 5 minutes
 1381 before each flare begins to 2.5 minutes after
 1382 the final flare cadence. Repeat Step 1 a final
 1383 time.

1384 The final step of flare identification and fitting was
 1385 performed using `altaipony` (Davenport 2016;
 1386 Ilin et al. 2021). The analytic flare model is from
 1387 Davenport et al. (2014) and it parametrizes the flare
 1388 with a start time, an exponential lag time, and an
 1389 amplitude.

1390 There were $N_f = 24$ flares that exceeded 0.5% in
 1391 relative flux during the short cadence observations.
 1392 These 24 flares spanned a total of 6.5 hours (~ 15
 1393 minutes per flare). Inspecting the data, we noticed
 1394 a coincidence in the flare arrival times. The co-
 1395 incidence is that despite the low flare duty cycle,
 1396 one orbital period after the brightest flare, a second
 1397 flare followed. This and a similar event are shown
 1398 in Figure 13. The timing error is good to a $\approx 0.2\%$
 1399 difference from the orbital period, which given the
 1400 duty cycle seems *a priori* unlikely. If we consider
 1401 flares falling within 2% of the planet’s orbital pe-
 1402 riod after a previous flare, then 4 of the 24 flare
 1403 events have candidate “successors”.

1404 As with any coincidence, if one does not have a
 1405 firm prediction, it is difficult to assess whether a
 1406 surprise is statistically significant. Since our sur-
 1407prise was specifically at the inter-arrival time of
 1408 certain flares coinciding with special time inter-
 1409 vals, we performed the following analysis. First,
 1410 we considered all unordered pairs of flares. For
 1411 N flares there are $\binom{N}{2}$ such pairs (for our case,
 1412 276 pairs). We then compared the distribution of
 1413 the pair separations against that of a Poisson dis-
 1414 tribution. Specifically, we drew $N_f = 24$ samples
 1415 from a Poisson distribution with $\lambda = \Delta t / N_f$, for
 1416 $\Delta t = 97.7$ days the total duration of the observa-
 1417 tions, and repeated the draw 10^3 times with unique
 1418 random seeds.

1419 Figure 14 shows the results. The vertical lines
 1420 in the figure show the planetary orbital period,
 1421 the synodic period $P_{\text{syn}} = (P_{\text{rot}}^{-1} - P_{\text{orb}}^{-1})^{-1}$, and lin-
 1422 ear combinations thereof. The tidal period (half
 1423 the synodic period) is not shown. The bins are
 1424 logarithmically spaced to give 100 bins between
 1425 the minimum and maximum ordinate values. The
 1426 gray bands express the range of values observed
 1427 from the Poissonian draws. While it does seem
 1428 like an odd coincidence for peaks in the observed
 1429 flare arrival time distribution to coincide with the
 1430 locations of these “special intervals”, the statisti-
 1431 cal evidence for a non-Poissonian process driving

1432 the flares does not seem especially overwhelming.
 1433 More quantitatively, the peaks observed at the or-
 1434 bital and synodic periods are within the $\pm 2\sigma$ range
 1435 of a Poissonian process, and those at $P_{\text{orb}} + P_{\text{syn}}$ and
 1436 $P_{\text{orb}} + 2P_{\text{syn}}$ are only slightly above this range. With
 1437 that said, future analyses of these data by investiga-
 1438 tors with more knowledge of this topic could very
 1439 well yield more quantitative insights. Such analy-
 1440 ses should keep in mind an important caveat: the
 1441 amplitude distribution of M-dwarf flares extends
 1442 up to many times the quiescent flux (see Figure 7 of
 1443 Günther et al. 2020). A flare on Kepler 1627B pro-
 1444 ducing double its quiescent white-light flux would
 1445 yield a $\approx 1\%$ apparent amplitude. Such flares could
 1446 represent a significant fraction of those in the Ke-
 1447 pler observations.

List of Changes

Replaced: ~~through~~ replaced with: **with**, on page [1](#).

Added: This also involved cuts on the photometric signal to noise ratio, the number of visibility periods used, the astrometric χ^2 of the single-source solution, and the $G_{\text{BP}} - G_{\text{RP}}$ color excess factor., on page [3](#), line [168](#).

Replaced: ~~agree reasonably well with~~ replaced with: **are within a factor of two of**, on page [3](#), line [184](#).

Replaced: ~~from~~ replaced with: **in**, on page [3](#), line [186](#).

Added: , and are all small enough that the choice of whether to use them *vs.* other extinction estimates does not affect our primary conclusions, on page [3](#), line [189](#).

Deleted: ~~hybrid~~ on page [5](#), line [219](#).

Replaced: ~~to~~ replaced with: **and**, on page [5](#), line [220](#).

Replaced: ~~s 6 and 7~~ replaced with: **6**, on page [5](#), line [221](#).

Added: To derive a probability distribution function for the age of δ Lyr cluster, we then assumed a Gaussian likelihood that treated the interpolated isochrones as the “model” and the δ Lyr cluster’s isochrone as the “data” (Equation 7 from [Gagné et al. 2020](#)). The cluster’s age and its statistical uncertainty are then quoted as the the mean and standard deviation of this age posterior., on page [5](#), line [223](#).

Added: As a matter of scope, we restricted our attention to the 391 stars discussed in Section [2.1](#) in the spatial and kinematic proximity of Kepler 1627. , on page [5](#), line [259](#).

Deleted: ~~As a matter of scope, we restricted our attention to the 391 stars discussed in Section [2.1](#) in the spatial and kinematic proximity of Kepler 1627.~~ on page [5](#), line [278](#).

Replaced: ~~these~~ replaced with: **our 391** , on page [5](#), line [283](#).

Added: **from each other**, on page [5](#), line [301](#).

Replaced: ~~The other stars are likely to be field contaminants.~~ replaced with: Although some of these outlier stars might be unresolved F+K binaries that are in the cluster ([Stauffer et al. 2016](#)), assuming that they are field contaminants provides a more secure lower bound of the rotation period detection fraction., on page [5](#), line [307](#).

Replaced: ~~renormalized unit weight error (RUWE)~~, replaced with: **RUWE**, on page [6](#), line [419](#).

Added: **(RUWE \approx 2.9; roughly the 98th percentile of the cluster’s distribution)**, on page [6](#), line [422](#).

Added: Given that the secondary companion’s brightness in the Kepler band is \approx 1.5% that of the primary, source confusion for the rotation signal is not expected to be an issue., on page [7](#), line [460](#).

Added: Based on Figure [1](#), the δ Lyr cluster may also be part of a similar hierarchical association., on page [21](#).

Added: **planetary** , on page [27](#).